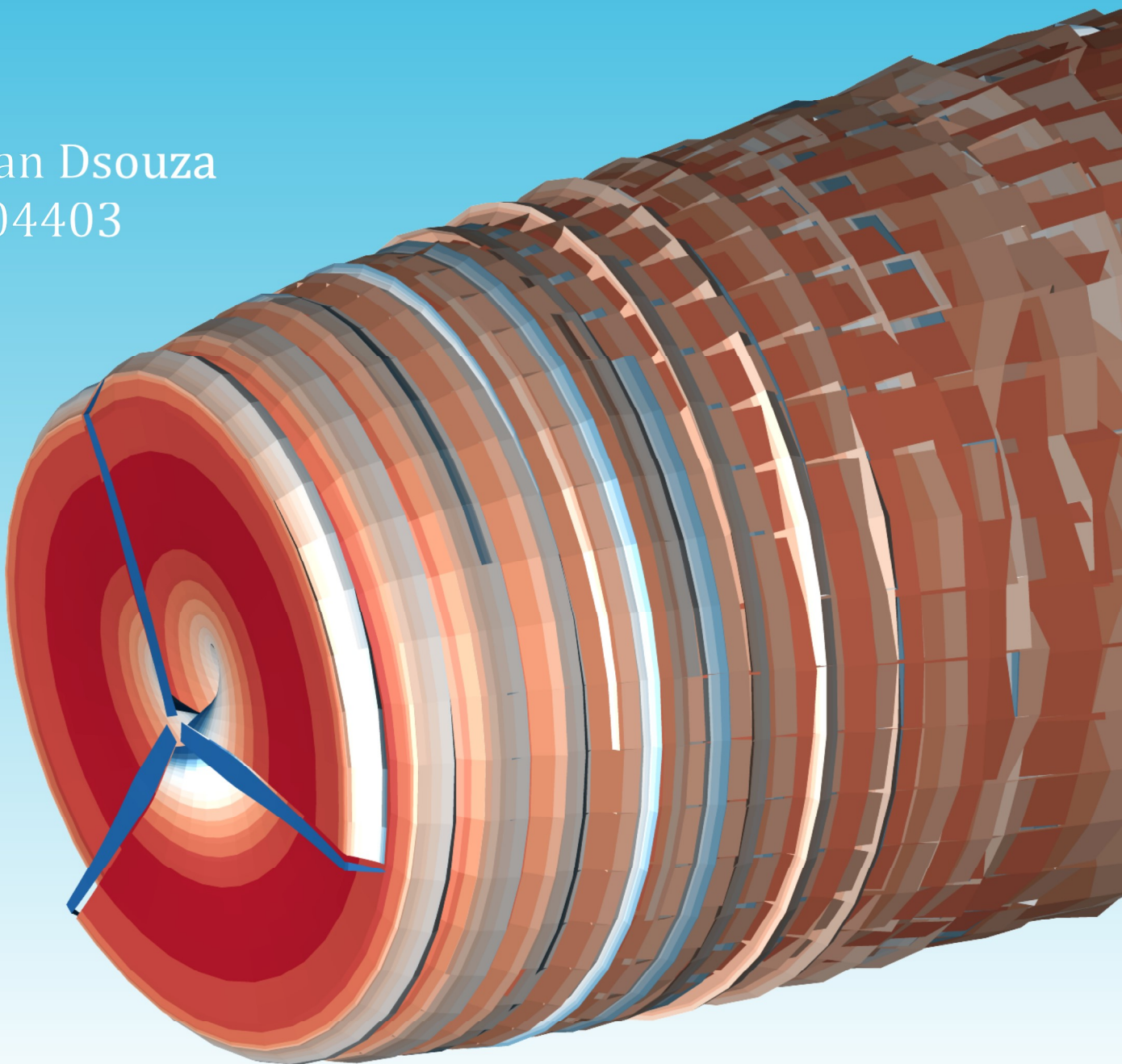M.Sc. Thesis in Aerospace Engineering

A Comparative Study to Assess the Accuracy of the Lifting Line Code AWSM for Simulating Winglets on Wind Turbines

Brian **Dsouza**
5004403

TUDelft

TNO
innovation
for life

A COMPARATIVE STUDY TO ASSESS THE ACCURACY OF THE LIFTING LINE CODE AWSM FOR SIMULATING WINGLETS ON WIND TURBINES

A thesis submitted to the Delft University of Technology in partial fulfillment
of the requirements for the degree of

Master of Science in Aerospace Engineering

by

Brian Dsouza

December 2021

ABSTRACT

Wind turbine power output has grown massively over the past few decades, and this has been achieved in part by increasing the size of rotors. But the size of rotors is now limited by structural constraints as well as space constraints in wind farms. It is therefore important to use other innovative methods to increase wind turbine capacity without increasing size. One way to achieve this is by the use of winglets. Winglets increase power output by reducing tip effects, thereby producing a more efficient distribution of forces over the blade. The art of designing winglets is to find the best trade-off between the increase in profile drag of the winglet itself and the reduction of induced drag that the winglet provides. To do this, it is very important to fully understand the aerodynamics of winglets on wind turbine blades.

High fidelity methods like Computational Fluid Dynamics (CFD) are capable of producing accurate and detailed flow fields and are able to offer greater insight into the complex aerodynamics of winglets on rotors. However, this comes at great computational cost which might be infeasible in the design and optimization of winglets. More common and cheaper models like the Blade Element Momentum (BEM) method are incapable of modelling winglets and other out-of-plane features. The Lifting Line Method is a middle ground that is capable of simulating winglets, but is also comparatively inexpensive.

The goal of this thesis is to study the performance of the Lifting Line method, in particular, ECN Aeromodule's AWSM Free-Wake Vortex Lifting Line code in simulating the case of winglets mounted on wind turbines. Aerodynamic Wind Turbine Simulation Module (AWSM) results are compared with results of normal and tangential forces and circulation distribution from a validated OpenFOAM model. The results show that over the outboard section of the blade and over the span of the winglet, AWSM performs well in predicting the performance of the blade-winglet configuration. This study shows that AWSM is a reliable tool for the design and optimization of winglets on wind turbine blades at a much lower cost than higher fidelity methods like CFD.

Keywords: Lifting-Line, CFD, Wind Turbine, Winglet, Aerodynamics, Free-Wake Vortex, RANS

ACKNOWLEDGEMENTS

CONTENTS

LIST OF FIGURES

LIST OF TABLES

LIST OF SYMBOLS

a	Induction Factor
a_B	Blade Induction Factor
$\bar{a}$	Annulus Averaged Induction Factor
b	Wing Span
c_i	Local Chord
C_D	Coefficient of Drag
C_f	Skin Friction Coefficient
C_L	Coefficient of Lift
$C_{L,\alpha}$	Lift Curve Slope
C_p	Coefficient of Pressure
D	Drag
D_i	Induced Drag
e	Span Efficiency Factor
$\vec{F}$	Force
F_c	Force wrt Local Chord
F_n	Normal Force
F_r	Force wrt Rotor Plane
F_t	Tangential Force
k	Turbulent Kinetic Energy
l_o	Vortex Filament Length
L	Lift
r	Distance from Vortex Filament
$rCurvi$	Length along Blade Span from Hub
R	Rotor Radius
TLF	Tip Loss Factor
U_∞	Freestream Velocity
$\vec{V}$	Velocity
w	Downwash
α	Angle of Attack
α_{eff}	Effective Angle of Attack
α_i	Induced Angle of Attack
Γ	Circulation
ε	Turbulence Dissipation Rate
ρ	Density
τ_{ij}	Shear Stress Tensor
ω	Specific Turbulence Dissipation Rate
Ω	Angular Velocity

ACRONYMS

1 | INTRODUCTION

The wind, being a source of clean, renewable energy, makes it an attractive alternative to fossil fuels. There has been rapid development of wind energy technology in the past two decades (Leung and Yang [2012]; Herbert et al. [2014]). The 2014 Danmarks Tekniske Universitet (DTU) International Energy report (Larsen and Petersen [2014]) predicts that up to 34% of the electricity demands of the European Union will be met by wind energy by 2030. Power output of wind turbines has grown massively from around 50kW in the 1980s to over 10MW today. This growth has spurred innovation in the design of wind turbines from noise reducing trailing edge serrations (Llorente and Ragni [2020]; Oerlemans [2016]) to the addition of winglets to the tips of wind turbine blades to increase power output (Johansen and Sørensen [2006]; Gaunaa and Johansen [2007]).

Winglets increase the power produced by a blade of a given length by reducing the induced drag at the tip of the blade, thereby increasing the efficiency of the rotor. Until recently, an increase in power generated by the rotor was achieved by simply making the blades longer. However, we are now reaching the structural limits of increasing the blade length, and because of space restrictions on wind farms, the use of winglets is becoming more common. It is therefore very important to fully understand the aerodynamics of winglets on rotor blades and to find the most efficient ways to analyze the performance of rotors mounted with winglets.

The flow-field around a winglet can be modeled using inviscid theory because a winglet alters the circulation around the tip of the blade, which has already been extensively studied over the past decades (Anderson Jr [2010]; Katz and Plotkin [2001]). The influence of the winglet is only on the outer part of the blade, and thus the viscous effects of the separated flow near the root of the blade does not have an effect on the performance of the winglet.

For the design and analysis of winglets, high-fidelity models like Computational Fluid Dynamics (CFD) are capable of resolving more of the flow physics and are thus more accurate. However, the higher fidelity comes at higher computational cost and time. This becomes infeasible for design iterations, and therefore there is a need for accurate lower-fidelity models. Blade Element Momentum (BEM) and actuator disk methods cannot handle out of plane geometries like winglets due to the underlying assumptions in their formulation. The Lifting-line method is capable of handling winglets and curved blades by representing the blade as lifting lines and computing the circulation that produces the same flow field as would have been produced by the actual blade. This method, combined with appropriate modelling of the wake (Van Garrel [2003]) can produce good results for blades without winglets. There is, however, limited research done to study the performance of the Lifting-line method for the case of a winglet-mounted blade in terms of distribution of local forces and circulation.

This thesis aims to study the performance of the lifting-line method for the application of analyzing the performance of a wind turbine with winglets mounted on the blade tips. A CFD model of the baseline model of the DanAero LM 38.8m blade will be developed on OpenFOAM and after validation, will be used to study the dif-

ferences in performance of the lifting line method when compared to CFD results. To achieve these research goals, the following research questions are formulated:

1. **What are the limits of validity of Lifting Line Methods for the simulation of winglet mounted wind turbines?**
   Literature study delving deep into the theory of the Lifting Line method paying attention to the assumptions made in the formulation and critically analyzing these assumptions in the presence of 3D effects around winglets mounted on wind turbine blades. The effects of these assumptions on the performance of the wind turbine will be quantified and compared to predictions made by CFD.

2. **How reliable are the predictions from the Lifting Line method?**
   A CFD model of the DanAero LM 38.8m wind turbine blade is developed on OpenFOAM. Baseline simulations on the unmodified blade will be performed and compared to the results from the Lifting Line method and reference data. Then, CFD simulations will be performed on the blade mounted with the winglet and a similar comparison will be performed with the Lifting Line results for the same configuration. Emphasis is given to the differences between the predictions of the Lifting-Line Theory (LLT) and CFD.

2 | AERODYNAMICS OF A WINGLET

This chapter discusses the aerodynamic phenomena around a winglet. First, the aerodynamics of an aircraft winglet will be explored and then, the discussion will be extended to the case of a rotating winglet, as in the case of a wind turbine blade. Aerodynamic theory of the winglet, along with the application of the Lifting Line method to winglets is explored along with recent advances in winglet aerodynamics.

2.1   AIRCRAFT WINGLET

Before considering the complex aerodynamics of rotor winglets, it is extremely important to fully understand the fundamentals of aerodynamics of aircraft winglets. The main purpose of a winglet is to displace and reduce the size of wing tip vortices (Nangia et al. [2006]). For the case of an aircraft winglet, i.e. a non-rotating winglet, this means a reduction in induced drag. An elegant way to explain induced drag is by representing the wing as lifting lines. Considering an isolated wing, this system consists of a bound vortex element fixed at a certain location along the span of the wing, a trailing vortex element at each wingtip, and a shed vortex (or starting vortex) advecting with the flow. This system is presented in Figure 2.1, extracted from Katz and Plotkin [2001].
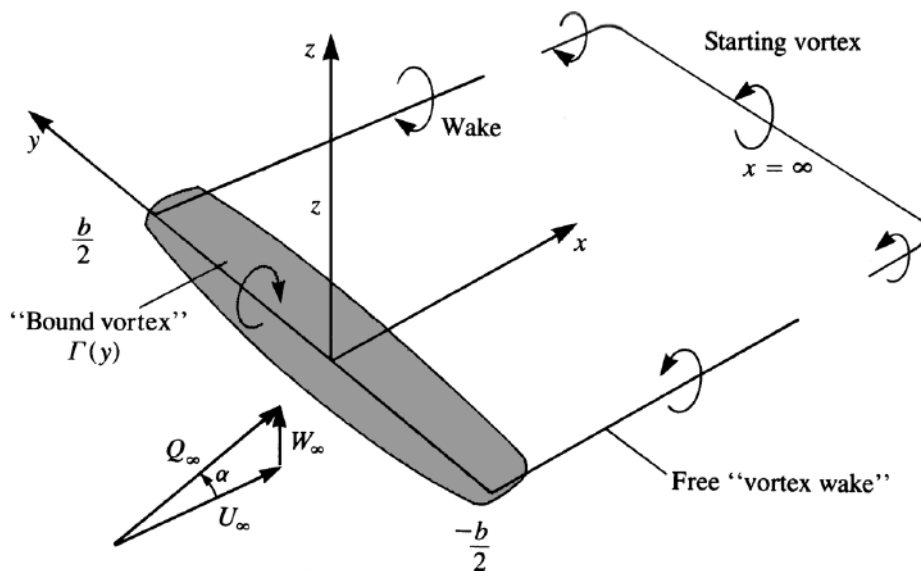
Figure 2.1: Vortex Filament System around a Finite Wing (Katz and Plotkin [2001])

The tip vortices and the starting vortex are a direct consequence of Helmholtz's second theorem, which states that a vortex filament cannot start or end in a fluid; it must extend to the boundaries of the fluid or form a closed path. The manifestation of this theorem is the closed path system of bound, tip, and starting vortices for an

isolated finite wing.

In the $y - z$ plane, the presence of the trailing vortex induces a flow-field that causes the flow to *leak* from the high pressure lower side to the low pressure upper side. The effect of this is to induce a velocity in a direction perpendicular to the free stream, and this causes a higher downwash at the tip. Under steady state conditions where circulation stays constant in time, the Biot-Savart law can be used to compute the flow downstream of the wing. This is written as

$$d\vec{V} = \frac{\Gamma}{4\pi} \frac{d\vec{l} \times \vec{r}}{|\vec{r}^3|} \tag{2.1}$$

The induced velocity at any point P at a distance of h for a semi-infinite vortex filament can be written as

$$V_P = \frac{\Gamma}{4\pi h} \tag{2.2}$$

The downwash resulting from the trailing tip vortex is computed using the Biot-Savart law as

$$w(y) = -\frac{\Gamma}{4\pi(b/2 - y)} \tag{2.3}$$

Equation 2.3, however, is problematic because there exists a singularity at $y = b/2$ (Figure 2.2). Infinite velocities at this point is nonphysical. This problem was overcome by Prandtl [1921] by considering a superposition of an infinite number of horseshoe vortex elements in place of a single horeshoe element, which results in the following downwash distribution

$$w(y_0) = -\frac{1}{4\pi} \int_{-b/2}^{b/2} \frac{(d\Gamma/dy)dy}{y_0 - y} \tag{2.4}$$
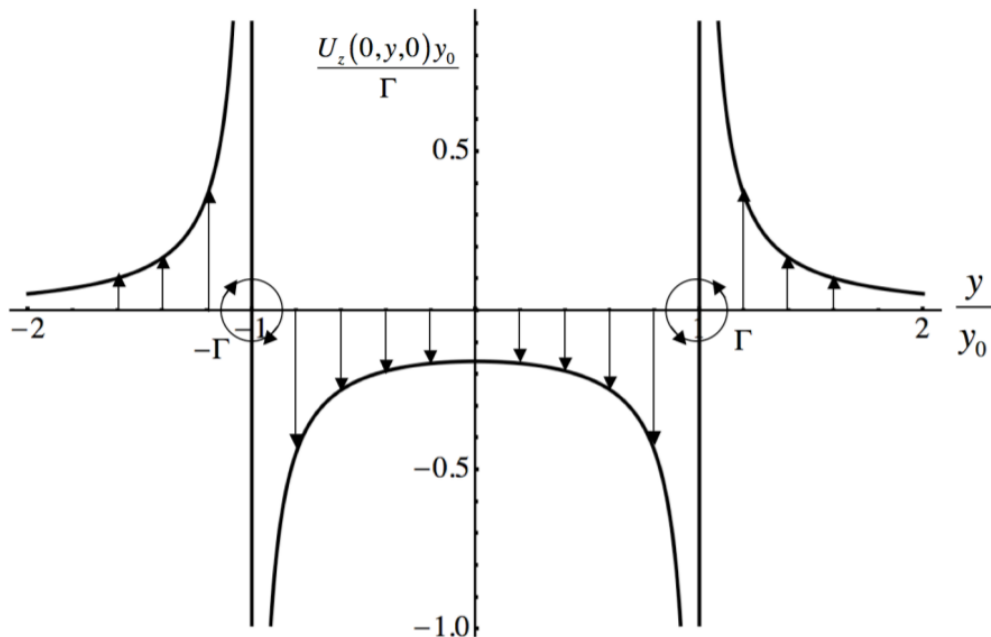
Figure 2.2: Downwash distribution over Finite Wing (Cantwell [2020])

According Prandtl's modified equation (Equation 2.4), one way to reduce downwash, thus reducing induced drag, is by somehow reducing the circulation gradient term ($d\Gamma/dy$) at the tip. The reduction of downwash causing the reduction of induced drag is explained as follows. The presence of downwash at a local section of the wing creates an induced angle of attack, which changes the direction of the effective lift force (Figure 2.3).
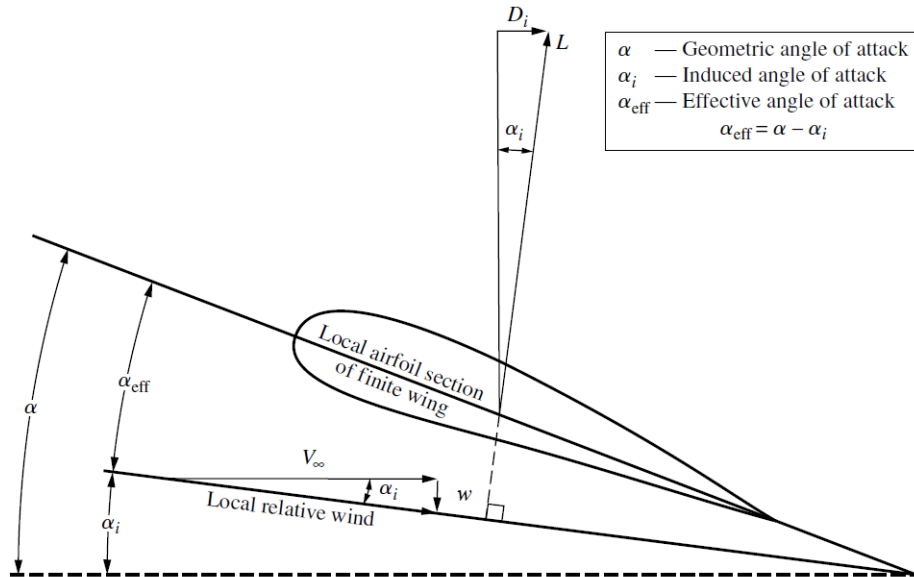
Figure 2.3: Effect of Downwash on the local flow over a section of a Finite Wing (Anderson Jr [2010])

The lift vector in the presence of downwash now tilts further backwards, which means there is a component of lift acting in the direction opposite to the freestream wind. This is called the induced drag. The overall result is that the lift is reduced and the drag is increased. Prandtl [1921] formulated an equation to compute the induced drag of a finite wing, given as

$$D_{ind} = \frac{L^2}{q\pi b^2 e} \tag{2.5}$$

where q is the chord, b is the span and e is the span efficiency factor. The span efficiency is maximum for the case where the lift distribution is elliptical ($e = 1$). Now, Equation 2.5 implies there are several ways induced drag can be reduced. The easiest was is to increase the span of the wing, because the induced drag is inversely proportional to the square of the span. This option is not always feasible because the design of the wing is subject to several constraints, span being one of them. A second way would be to design a wing such that the span efficiency is maximum. Anderson Jr [2010] provides an analysis of Equation 2.4 that shows that an elliptical lift distribution, with the maximum span efficiency factor, is obtained when the chord distribution is also elliptical. This has been implemented in some designs, most notably on the Supermarine Spitfire.

Non-planar wings are another way to reduce induced drag over a finite wing. There are several design possibilities for non-planar wings and Kroo [2005] used Trefftz Plane Analysis (Drela [2014]) to compute the span efficiency factors of many of these designs (Figure 2.4).

The analysis by Kroo [2005], however, does not say anything about skin-friction drag. This means that, for example, the most efficient non-planar wing - the box
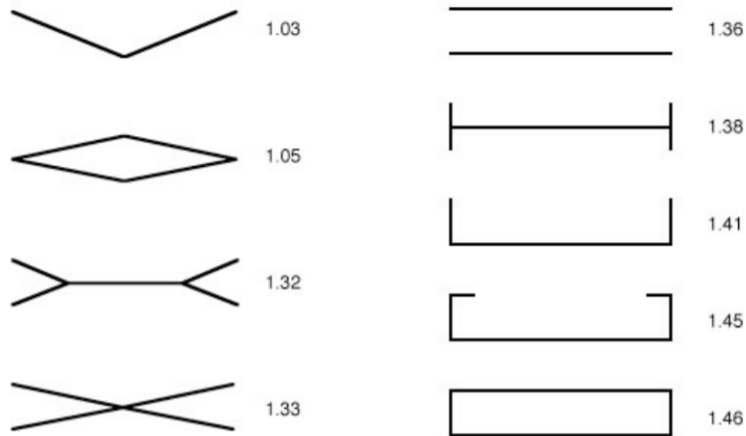
Figure 2.4: Span Efficiency Factors for Non-Planar Wings (Kroo [2005])

wing - having a span efficiency factor of $e = 1.46$ will have a much higher skin-friction drag, thus defeating the whole purpose of the design. An optimization study by Gage [1995] including profile drag as well as induced drag, under constraints for lift, span, and height found that the C-shape wing shows the most promising performance. This design is the traditional vertical winglet configuration which is simple and shows the most promise in reducing induced drag.

An explanation for the reduction of induced drag for this wing-winglet configurations using Lifting Lines can be done as follows. The winglet moves the tip trailing vortex away from the main wing (Figure 2.5). The trailing vortex is now physically further away from the main wing, thus, the effects of velocities induced by the trailing vortex is lower. The smaller induced velocities seen by the wing mean a lower induced angle is seen by the wing. Because of this, a smaller component of the Lift vector points in the direction opposite to the freestream, resulting in lower induced drag.
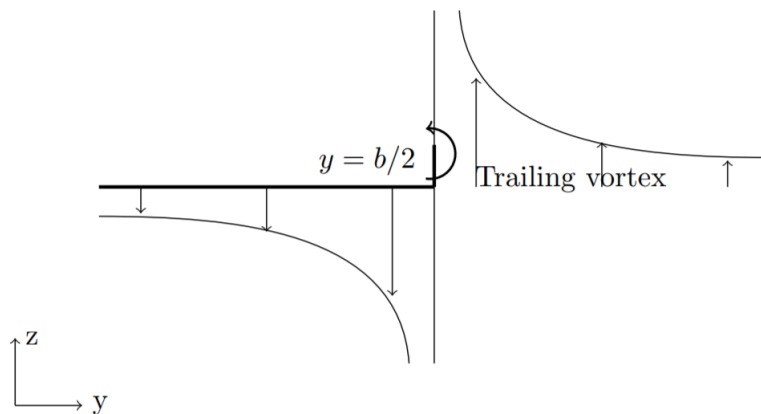
Figure 2.5: Downwash Distribution around a Wing-Winglet Configuration (Leenders [2021])

2.2 ROTATING WINGLET

Now that a good understanding of the aerodynamics of winglets for aircraft applications has been developed, this will be extended to the case of rotating winglets,

such as those on wind turbines. Salient differences between the rotating winglet and non-rotating winglets are elaborated on.

A first approach to study the aerodynamics on wind turbines is the Actuator Disk theory, based on the 1D momentum theory. In the actuator disk theory, the wind turbine is replaced by a porous *actuator disk*, which extracts energy from the freestream. The actuator disk exerts a force on the flow, and this force can be used to compute the power extracted by the wind turbine by multiplying with the freestream velocity. Gaunaa and Johansen [2007] extend this idea of the actuator disk to account for the winglets on a wind turbine. This extension is called the Actuator Cap theory Figure 2.6). The actuator cap theory is based on the assumptions of an infinite number of blades and assume the total bound vorticity on the cap to be constant. This means that vorticity is shed from the root and tips only.

Figure 2.6: The Actuator Cap Model with the actuator cap shown in black and the trailing vortices shown in blue (Gaunaa and Johansen [2007])

They show that because all axial and radial induction in the case of the actuator cap comes only from the outer vortex sheet (Øye [1990]) and because of its resulting implications, applying the conservation of mass equation to the actuator cap theory gives exactly the same result as that when the conservation of mass equation is applied to the actuator disk theory. These two theories both assume infinite number of blades, and thus do not have tip effects. As a result, in the absence of tip effects, adding winglets does not increase power production. Further, this implies that the positive effect of winglets arises from the reduction of tip effects. This also means that the Betz limit still applies for the wind turbine with winglets and limits the maximum Coefficient of Power (CP) that can be obtained.

This is in contradiction the classical explanations for the positive effects of winglets on wind turbines of Van Bussel [1990] who used momentum theory on the same problem and concluded that power augmentation with the use of winglets was due to the downwind shift of vorticity. Upon further inspection of Van Bussel [1990]'s method, it becomes apparent that the terms accounting for power production by the winglets were not included in the first place (Gaunaa and Johansen [2007]).
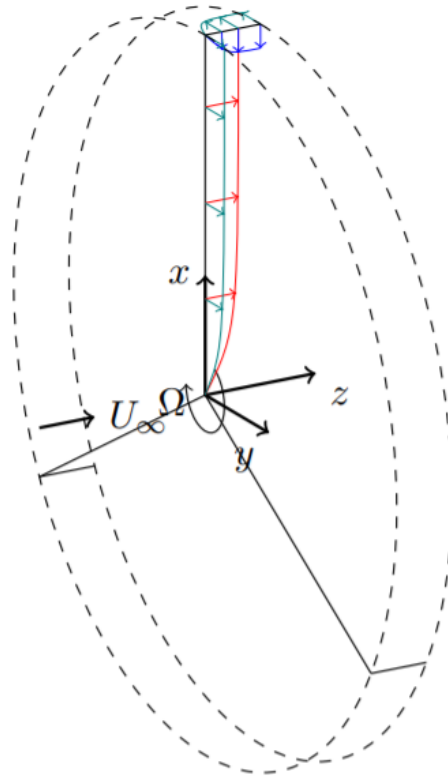
Figure 2.7: A Lifting Line Description of a Wind Turbine with Winglets (Based on Gaunaa and Johansen [2007] and taken from Leenders [2021])

A lifting line description of the wind turbine with winglets is presented in Figure 2.7 (Leenders [2021]). Using this description and by using the Kutta-Joukowski theorem:

$$\vec{L} = \rho V_{rel} \times \vec{\Gamma} \tag{2.6}$$

the system forces acting on the blade and the winglet can be described as follows

$$\vec{F}_{blade} = \rho\Gamma \begin{bmatrix} 0 \\ U_\infty + u_{ind} \\ \Omega z - v_{ind} \end{bmatrix} \tag{2.7}$$

$$\vec{F}_{winglet} = \rho\Gamma \begin{bmatrix} \Omega z + v_{ind} \\ -w_{ind} \\ 0 \end{bmatrix} \tag{2.8}$$

where the subscript *ind* means induced velocity in the corresponding direction and the forces are in the order: radial forces, tangential forces, axial forces. The winglet forces shown here are based on Figure 2.7 for a downwind winglet. In the case of an upwind winglet, the signs of the forces are reversed. Similar to the non-rotating case, the presence of the winglet shifts the trailing tip vortex out of the plane of the rotor (upwind or downwind depending on winglet configuration) which causes a reduction in tip effects.

Imamura et al. [1998] were one of the first to use the Lifting Line Method to investigate winglets on wind turbine blades. Using the Free Wake model, they showed

that there is indeed an enhancement in the power production of wind turbines by using winglets. They also explained the increase in wind turbine efficiency is because of an increase in the mass flow rate through the rotor, and due to an increase in circulation near the blade tip because of lower axial induced velocities. Gaunaa and Johansen [2008] used a Free Vortex Lifting Line method to quantify the increase in aerodynamic effects of wind turbines with the use of winglets. Their results show an increase a power output of 2.2% for a 2% winglet. These results were also compared to CFD simulations, which showed that the Lifting Line method can relatively accurately predict integral quantities like power increase with the use of winglets. Lawton and Crawford [2014] performed a similar study with the lifting line method showing similar results as Gaunaa and Johansen [2008] and add that the increase in thrust is also accurately predicted. Another study performed by Gaunaa et al. [2011] uses a new computationally efficient algorithm for non-straight blades to study in detail the Free Wake and Prescribed Wake Lifting Line methods. It was shown that the computationally more expensive Free Wake method performed generally well when compared to CFD results, with the Prescribed Wake method producing good results in cases similar to ones they were calibrated for. A study on winglets in complex inflow conditions such as turbulence and shear was conducted by Sessarego et al. [2018] and it was shown that under complex inflows, short swept blade tips and winglets performed better, because they produced lower loads on the turbine.

In parallel, there have been several CFD studies investigating the effects of winglets on wind turbines. Johansen and Sørensen [2006] investigated the effect of upstream and downstream winglets and the effect of winglet twist using Risø/DTU's EllipSys3D incompressible Navier-Stokes solver. All the winglets tested had a cant angle of 90°. In their study, they confirmed the result that winglets increase power production on wind turbines, with higher increase in power at higher speeds while keeping the rotor speed constant. It was also seen that the twist distribution of the winglet also had a significant effect on power production. An increase in thrust was also seen on all winglet designs studied, with downwind winglets showing a higher increase in thrust compared to upwind winglets.

Johansen and Sørensen [2007] also studied the effect of winglet height, radius of curvature at the root, and sweep on the power production of wind turbines. It was seen that thrust and power production of the wind turbines increased with increasing winglet height, as was expected. As for the radius of curvature at the root of the winglet, it was seen that a higher power increase was observed for smaller radii of curvature. Sweep seemed to have a negligible effect on the power production of the turbine. Ferrer and Munduate [2007] studied the effect of different winglet shapes using CFD showing that under attached flow conditions, tip shapes modify the radial component of the flow leading to 3D effects that affect local loading of the blade and winglet. It was also shown that high aspect ratio winglets have larger increase in power production per unit thrust. Gaunaa and Johansen [2007] found that the power increase for small winglets is similar to a simple extension of the blade of the same length. Conclusions by Khaled et al. [2019] for a 45° winglet seem to show that this configuration produces a larger power increase, but because the winglets considered were small, the power production for the 45° winglet can be analogously explained by Gaunaa and Johansen [2007]'s conclusions. A study by Kalvig et al. [2014] comparing several different wind turbine aerodynamic models using CFD shows that the actuator disk method could successfully and accurately calculate the far wake of the wind turbine, thus offering a cheaper alternative to fully resolved CFD in studying wind turbine wakes. However, they also showed that the fully resolved blade yielded superior results in terms of force predictions, justifying the added cost of such a method. From several studies using various turbulence models, it was observed that the $k - \omega$ SST consistently showed better performance for the application to wind turbines (Muiruri et al. [2019]), but RANS

models in general struggle to accurately capture complex flow fields near the tip vortex at high speeds. A different approach taken by Zahle et al. [2018] using CFD-based surrogate models show that optimal winglets can be designed without significantly increasing the overall thrust. In their case, an increase in power of 2.6% was observed with minimal increase in thrust. Garcia-Ribeiro et al. [2021] performed an in-depth parametric study on winglet design using CFD, and confirmed the earlier observations that the positive effect of winglets was by weakening the strength of the tip vortex and showed that the winglets made the pressure distribution over the upper surface of the blade more favourable for the generation of lift. They conclude that the efficiency of winglets improve consistently with lower taper ratios and lower root chord ratios under moderate wind speeds.

Much of the literature discussed in this chapter focuses on the overall power and thrust increase with the use of winglets on wind turbines. However, there is very limited literature on how the distributed loads and circulation vary over the span of the blade and the winglet and what exactly happens at the junction of the winglet and the blade. With this thesis, an attempt is made to assess how well the Lifting Line method is able to capture the distributed quantities when compared to high fidelity CFD data.

3 | NUMERICAL TOOLS

This chapter describes the ideas and theory behind the numerical tools used in this thesis for the study of the aerodynamics of winglets on wind turbines. The basic ideology and the particular implementation of these methods are discussed along with recent advances in the state of the art.

3.1 LIFTING LINE METHOD

Lifting-line theory is based on two of Prandtl's fundamental ideas: the wing-section characteristics can be treated using two-dimensional theory, and the three-dimensional tip effects are taken into account by calculating the effective angle of attack. In the study of potential flow, the physical flow around a body can be represented as the velocity field induced by a distribution of vortices or sources combined with a uniform freestream flow (Reid and Hunsaker [2021]; Anderson Jr [2010]; Prandtl [1921]). The Lifting-line method uses a distribution of lumped vortex filaments combined with a uniform flow to model real world flows. The method computes the unknown circulation distribution that produces an induced flow field along the quarter chord of the wing resulting in the same lift distribution as the physical flow for a given freestream condition.

3.1.1 Prandtl's Lifting–line Theory

In the classical implementation of the Lifting-line method by Prandtl (Anderson Jr [2010]), the circulation $\Gamma(z)$ is computed by equating the sectional lift coefficient using the Kutta-Joukowski theorem and using the assumption that the sectional lift distribution is a linear function of the angle of attack.

According to the Kutta-Joukowski theorem, the sectional lift is given by

$$C_L = \frac{2\Gamma}{V_\infty c} \tag{3.1}$$

where c is the local chord length and V_∞ is the freestream velocity. Additionally,

$$C_L = C_{L,\alpha}(\alpha_{eff} - \alpha_{L,0}) \tag{3.2}$$

where $C_{L,\alpha}$ is the lift curve slope, $\alpha_{L,0}$ is the zero-lift angle of attack, which are both properties of the airfoil and α_{eff} is the effective angle of attack. Assuming a small induced velocity compared to the freestream value, the relationship between the global angle of attack and the effective angle of attack is given by

$$\alpha_{eff}(z_0) = \alpha - \frac{1}{4\pi V_\infty} \int_{-b/2}^{b/2} \frac{(d\Gamma/dz)}{z_0 - z} dz \tag{3.3}$$

where z_0 is a spanwise location along the wing (Figure 3.1)
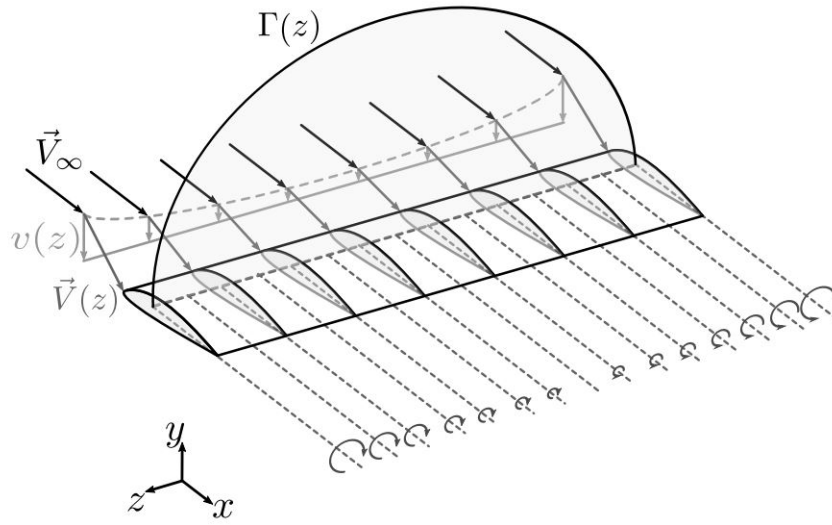
Figure 3.1: Schematic of Prandtl's Classical Lifting-line Theory (Reid and Hunsaker [2021])

Combining Equation 3.1, Equation 3.2, and Equation 3.3, we get an equation for the spanwise distribution of angle of attack as

$$\alpha(z_0) = \frac{2\Gamma(z_0)}{V_\infty c(z_0)C_{L,\alpha}(z_0)} + \alpha_{L,0}(z_0) + \frac{1}{4\pi V_\infty}\int_{-b/2}^{b/2}\frac{(d\Gamma/dx)}{z_0 - z}dz \tag{3.4}$$

Here, the circulation distribution $\Gamma(z_0)$ is the only unknown and the other terms are properties of the wing. Using a change of variables:

$$z = -\frac{b}{2}cos(\theta) \tag{3.5}$$

$$dz = \frac{b}{2}sin(\theta) \tag{3.6}$$

the general circulation distribution $\Gamma(z_0)$ can be expressed in terms of θ as a Fourier Sine Series.

$$\Gamma(\theta) = 2bV_i\infty\sum_{n=1}^{\infty}A_n sin(n\theta) \tag{3.7}$$

Differentiating Equation 3.7 wrt z, the spanwise coordinate, we get

$$\Gamma'(z) = \frac{d\Gamma}{dz} = \frac{d\Gamma}{d\theta}\frac{d\theta}{dz} = 2bV_\infty\sum_{n=1}^{\infty}nA_n cos(n\theta)\frac{d\theta}{dz} \tag{3.8}$$

The Fourier coefficients A_n are computed by solving Equation 3.4 at N locations along the span. This sets up a system of N equations to compute the first N Fourier coefficients of the circulation distribution. Using these coefficients, the circulation distribution is computed, which is then used to compute the entire flow field.

3.1.2 ECN Aero–Module: AWSM

AWSM is a tool within the Energy Research Center of the Netherlands (ECN) Aero-Module software for the simulation of wind turbine aerodynamics using the generalized lifting-line theory (Van Garrel [2003]; Grasso et al. [2011]). In this model, the lift generated by each section of a lifting surface acts at the quarter chord point and is computed using the local flow direction. A consequence of this implementation is that flow simulation is restricted to slender, high aspect ratio geometries, with minimal 3D effects. Viscosity is accounted for from the user-supplied sectional airfoil polars. The model is formulated for local flow velocities much smaller than the speed of sound such that the flow can be considered to be incompressible.

According to the analysis presented by Katz and Plotkin [2001] and Saffman [1995], the total force exerted by the fluid on a body is given as

$$\vec{F} = \int \int \int \rho(\vec{u} \times \vec{\omega})dV \tag{3.9}$$

where $\vec{\omega}$ is the vorticity defined as

$$\vec{\omega} = \vec{\nabla} \times \vec{u} \tag{3.10}$$

Considering a vortex line element $\vec{dl}$, the above equation becomes

$$d\vec{L} = \rho(\vec{u} \times \vec{\Gamma})dl = \rho\Gamma(\vec{u} \times \vec{dl}) \tag{3.11}$$

For a volume distribution of vorticity, the velocity field can be calculated by

$$\vec{u}_{\omega}(\vec{x}_p) = \frac{1}{4\pi} \int \int \int \frac{\vec{\omega} \times \vec{r}}{r^3}dV \tag{3.12}$$

where $\vec{x}_p$ is the evaluation point and

$$\vec{r} = \vec{x}_p - \vec{x} \tag{3.13}$$

$$r = \sqrt{\vec{r} \cdot \vec{r}} = |\vec{r}| \tag{3.14}$$

For a line vortex element, the velocity field is given by the Biot-Savart law

$$\vec{u}_{\Gamma}(\vec{x}_p) = -\frac{1}{4\pi} \int \Gamma \frac{\vec{r} \times \vec{dl}}{r^3} \tag{3.15}$$

Now, for a straight-line element with a constant vortex strength Γ, the velocity field can be computed analytically as (Phillips and Snyder [2000])

$$\vec{u}_{\Gamma}(\vec{x}_p) = \frac{\Gamma}{4\pi} \frac{(r_1 + r_2)(\vec{r_1} \times \vec{r_2})}{r_1 r_2(r_1 r_2 + \vec{r_1} \cdot \vec{r_2})} \tag{3.16}$$

Figure 3.2 shows the definition of the vectors $\vec{r_1}$ and $\vec{r_2}$ and the other parameters.
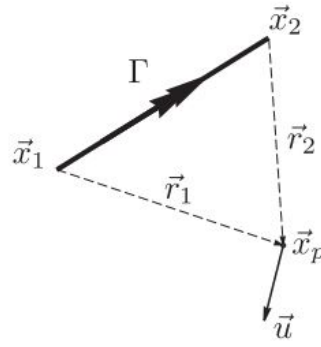
Figure 3.2: Vortex line geometry (Van Garrel [2003])

Equation 3.16 becomes singular when the evaluation point comes close to the vortex line itself. This behaviour is undesirable and therefore a certain cut-off radius parameter δ is introduced. The equation then becomes

$$\vec{u}_\Gamma(\vec{x}_p) = \frac{\Gamma}{4\pi} \frac{(r_1 + r_2)(\vec{r_1} \times \vec{r_2})}{r_1 r_2(r_1 r_2 + \vec{r_1} \cdot \vec{r_2}) + (\delta l_0)^2} \tag{3.17}$$

where l_0 is the length of the vortex filament. This ensures that the velocity smoothly approaches zero as the evaluation point approaches the vortex filament. The influence of a small cut-off radius is strongly felt near the vortex filament in the smooth implementation (Figure 3.3 taken from Van Garrel [2003])
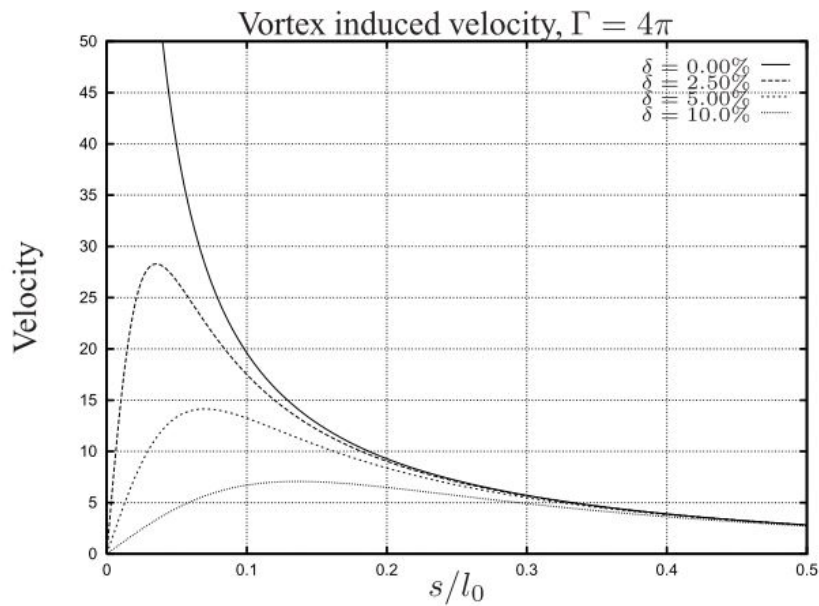
Figure 3.3: Vortex line velocity, smooth cut-off (Van Garrel [2003])

AWSM also implements a linear cut-off radius such that the velocity linearly deceases to zero within the cut-off radius (see Figure 3.4).
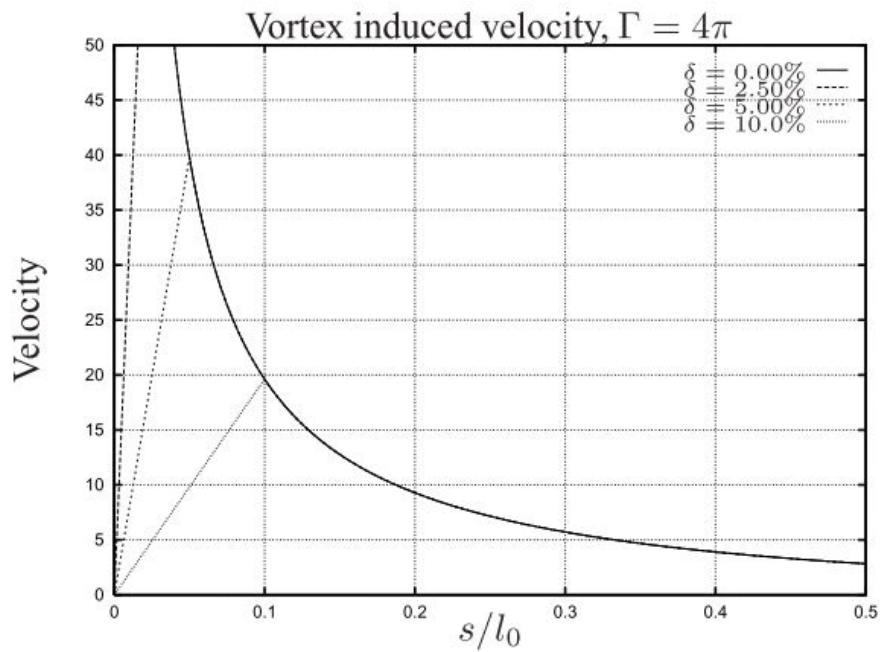
Figure 3.4: Vortex line velocity, linear cut off (Van Garrel [2003])

The wake structure is computed by AWSM from the shed vorticity of the vortex rings of each bound vortex element by convecting the vortex ring downstream with each time step. The strengths Γ of these vortex rings are computed at each time step Δt and are shed and joined to the shed vortex rings from the previous time steps, thus creating a vortex lattice structure (see Figure 3.5 - taken from Van Garrel [2003]).
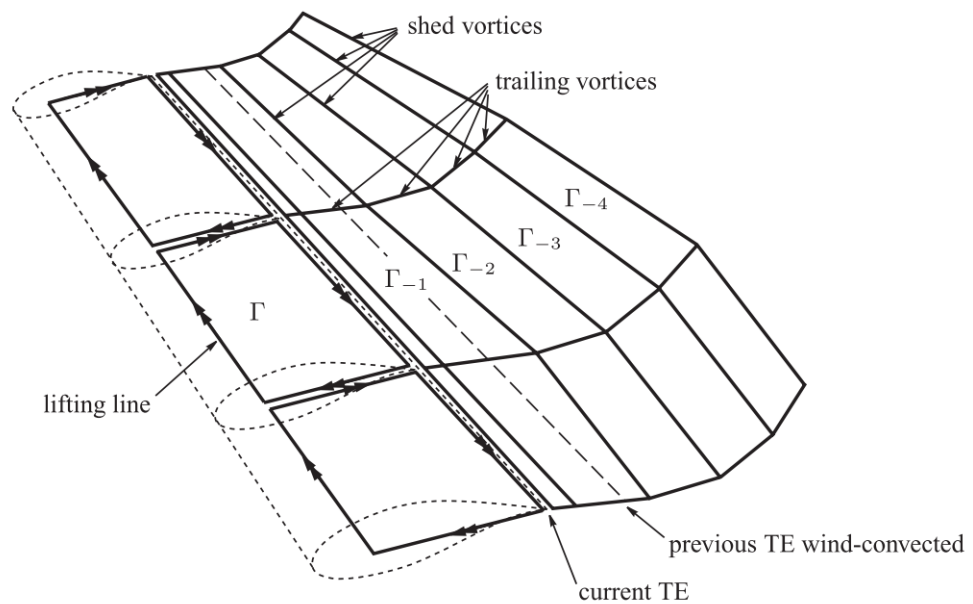
Figure 3.5: Wake Structure Computed by AWSM (Van Garrel [2003])

As per convention used for vortex lattice methods, the position of the first shed vortex ring is placed 25% of the local chord behind the trailing edge of the blade.

The downstream position is calculated for each time step and is the result of two separate effects. The first is the effect of convection by the wind and the second is the effect of convection by velocities induced by the vortex system of all bound and trailing vortex elements. The position of the shed vortex is calculated by summing up both these effects.

$$\Delta \vec{x} = \vec{u}_{wind} \Delta t \tag{3.18}$$

$$\Delta \vec{x} = \vec{u}_\Gamma \Delta t \tag{3.19}$$

The computation of vortex strengths is a non-linear problem because the lift over a blade section, and thus the circulation, is dependent on the local flow (the angle of attack experienced by the blade section). This circulation is the fixed vortex strength of that particular blade section. At the same time, the vortex line at this blade section also acts on the entire flow field. This means that it will influence the local flow field, and hence, the angle of attack experienced by the blade section. Therefore, an iterative solution method is selected to compute a converged vortex strength distribution. The problem is set up as follows (refer to Van Garrel [2003] for detailed formulation).

The lift force experienced by the local blade section is a function of the coefficient of lift, which is extracted from the user-supplied airfoil data, which is dependent on the local flow field (AoA). This lift force is written as

$$dL = C_l(\alpha) \frac{1}{2} \rho U^2 dA \tag{3.20}$$

where U is the local flow velocity and dA is the blade strip area. Now, the strength of the local vortex element can be calculated using Equation 3.11. Expressing the lift force due to the vortex element in a plane defined by the local chordwise and strip normal directions (Figure 3.6) we get:

$$dL_\Gamma = \rho \Gamma \sqrt{\left((\vec{u}_{cp} \times \vec{dl}) \cdot \vec{a}_1 \right)^2 + \left((\vec{u}_{cp} \times \vec{dl}) \cdot \vec{a}_3 \right)^2} \tag{3.21}$$

where $\vec{u}_{cp}$ is the local onset velocity at the control point of the blade section. It is composed of three velocities, namely, the oncoming wind, velocity due to rotation, and velocity induced by the vortex element.

In a similar way, expressing the lift force due to the local flow in the same coordinate system, we get:

$$dL_\alpha = C_l(\alpha) \frac{1}{2} \rho \left((\vec{u}_{cp} \cdot \vec{a}_1)^2 + (\vec{u}_{cp} \cdot \vec{a}_3)^2 \right) dA \tag{3.22}$$

Now, combining Equation 3.21 and Equation 3.22 and rearranging, we end up with:

$$\Gamma_{cl} = C_l(\alpha) \frac{\frac{1}{2} \left((\vec{u}_{cp} \cdot \vec{a}_1)^2 + (\vec{u}_{cp} \cdot \vec{a}_3)^2 \right) dA}{\sqrt{\left((\vec{u}_{cp} \times \vec{dl}) \cdot \vec{a}_1 \right)^2 + \left((\vec{u}_{cp} \times \vec{dl}) \cdot \vec{a}_3 \right)^2}} \tag{3.23}$$

This nonlinear system is solved using an algorithm that iteratively solves for Equation 3.23. The algorithm is briefly presented below (Van Garrel [2003])
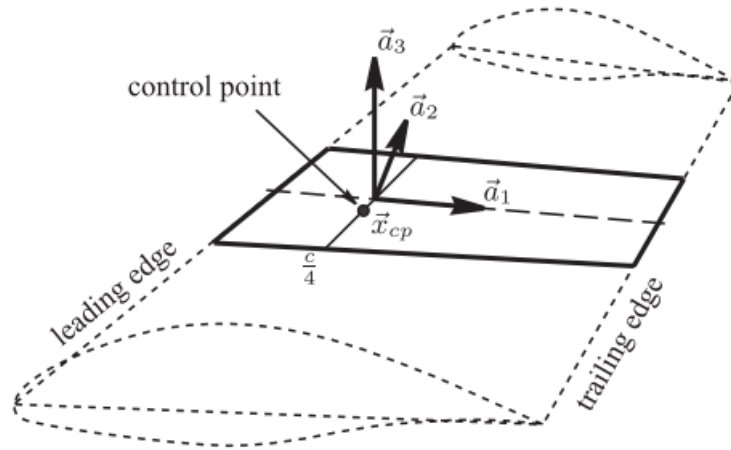
Figure 3.6: Geometry Definition of the Blade Section (Van Garrel [2003])

Algorithm 1 Algorithm to Compute Vortex Line Strengths (Van Garrel [2003])

1: Guess a distribution of blade strip vortex strengths Γ_j
2: Compute onset velocity $\vec{u}_{cp}$ at the control point of each blade strip
3: Compute local angle of attack α for each blade strip
4: Extract local lift coefficient by linear interpolation of aerodynamic data table using α
5: Using Equation 3.23, compute updated guess values for vortex strengths Γ_{cl}
6: Compute difference between current vortex strip strengths and updated guess values of vortex strengths

$$\Delta\Gamma = \Gamma_{cl} - \Gamma_j \tag{3.24}$$

7: Compute new blade strip vortex strengths using the previously computed $\Delta\Gamma$ and an underrelaxation factor θ

$$\Gamma_j = \Gamma_j + \theta\Delta\Gamma \tag{3.25}$$

8: Assess convergence. Repeat if vortex strength difference is larger than threshold value

---

3.2 COMPUTATIONAL FLUID DYNAMICS

Computational Fluid Dynamics is widely used in engineering analysis and design. It solves the governing differential equations on a discretized spatial domain to approximate real flow physics. The Finite Volume Method is the most common numerical method used to solve the discretized Navier-Stokes equations in most commercial CFD solvers. CFD can be used to achieve highly accurate results, but this comes at the cost of large computation times and high computational power requirements. This section provides an overview of the governing equations of fluid dynamics, turbulence modeling, Reynolds-Averaged Navier-Stokes (RANS) and Large Eddy Simulation (LES) approaches applied to wind turbines.

3.2.1 Governing Equations of Fluid Dynamics

From a macroscopic/continuum lens, the equations that govern fluid flow are the Navier-Stokes equations, which elegantly describe the conservation of mass, mo-

mentum, and energy. The equations will be presented in this chapter in their conservation form, i.e. from the Eulerean point of view, with a control volume fixed in space and the fluid flowing through it. The conservation of mass is described by the continuity equation as follows

$$\frac{\partial \rho}{\partial t} + \frac{\partial}{\partial x_j}(\rho u_j) = 0 \tag{3.26}$$

Equation 3.26 states that the time rate of change of the mass of the fluid element is zero. The conservation of momentum equation is obtained by applying Netwon's second law to the fluid control volume:

$$\frac{\partial}{\partial t}(\rho u_i) + \frac{\partial}{\partial x_j}(\rho u_i u_j + p\delta_{ij} - \tau_{ij}) = \rho g_i \tag{3.27}$$

where ρg_i represents body forces acting on the fluid. For Newtonian fluids, the shear stress in a fluid is proportional to its strain rate and is given by

$$\tau_{ij} = \mu \left(\frac{\partial u_i}{\partial x_j} + \frac{\partial u_j}{\partial x_i} \right) - \frac{2}{3}\mu \frac{\partial u_k}{\partial x_k}\delta_{ij} \tag{3.28}$$

Similarly, applying an energy balance to the finite control volume, one obtains the energy equation, given as:

$$\frac{\partial}{\partial}(\rho E) + \frac{\partial}{\partial x_j}(\rho u_j E + u_j p + q_j - u_j \tau_{ij}) = \rho g_j u_j \tag{3.29}$$

where q_j is the heat flux. The continuity equation, the three momentum equations, and the energy equation comprise of an under-determined set of five equations with six unknowns. The equation of state is used to close the system and solve for the last unknown. For high Reynolds number flows, the effect of viscosity becomes negligible compared to the inertial forces, and the system can be reduced to the so-called Euler equations.

$$\frac{\partial}{\partial x_j}(\rho u_j) = 0 \tag{3.30}$$

$$\frac{\partial}{\partial t}(\rho u_i) + \frac{\partial}{\partial x_j}(\rho u_i u_j + p\delta_{ij}) = 0 \tag{3.31}$$

$$\frac{\partial}{\partial t}(\rho E) + \frac{\partial}{\partial x_j}(\rho u_j E + u_j p) = 0 \tag{3.32}$$

The above set of equations are applicable when there are no body forces acting on the fluid and there is no heat flux. However, the Euler equations cannot predict complex flow phenomena like flow separation or boundary layer flow due to the lack of viscosity modelling, and is therefore not a useful tool for aerodynamic analyses of wind turbines. The full Navier-Stokes equations will be considered henceforth. It is sometimes useful to represent the Navier-Stokes equations in the vorticity form since turbulent flows show large fluctuations in vorticity (such as in separated flows and turbulent boundary layers). The vorticity form of the Navier-Stokes equations is obtained by taking the curl of the momentum equation.

$$\frac{D\omega_i}{Dt} = \omega_j \frac{\partial v_i}{\partial x_j} - \omega_j \frac{\partial v_j}{\partial x_i} + \varepsilon_{ijk}\frac{1}{\rho^2}\frac{\partial \rho}{\partial x_j}\frac{\partial p}{\partial x_k} + \varepsilon_{ijk}\frac{\partial}{\partial x_j}\left(\frac{1}{\rho}\frac{\partial \tau_{km}}{\partial x_m} \right) + \varepsilon_{ijk}\frac{\partial F_k}{\partial x_j} \tag{3.33}$$

where F_k is the summation of external body forces, ε_{ijk} is the permutation symbol, and τ is the viscous stress tensor.

3.2.2 Turbulence Modelling

One practical way to apply the Navier-Stokes equations numerically for the simulation of real world problems, like Wind Turbines, is to perform a Reynolds-averaging procedure. The idea is to decompose a quantity into its mean and fluctuating component. This decomposition is called the Reynolds decomposition. For example, performing Reynolds decomposition on velocity gives:

$$u(x,y,z,t) = \overline{u(x,y,z)} + u'(x,y,z,t) \tag{3.34}$$

Here, the over-bar denotes a time averaged (or ensemble averaged) quantity, which is therefore independent in time, and the prime denotes a quantity fluctuating around the mean. Applying the Reynolds decomposition to the momentum equation and then performing the Reynolds averaging, we get:

$$\rho \left(\frac{\partial \overline{u_i}}{\partial t} + \frac{\partial}{\partial x_j}(\overline{u_i u_j}) \right) = -\frac{\partial \overline{p}}{\partial x_j} + \frac{\partial \overline{\tau_{ij}}}{\partial x_j} - \frac{\partial}{\partial x_j} \left(\rho \overline{u_i' u_j'} \right) \tag{3.35}$$

As a result of Reynolds-averaging, Equation 3.35 has an additional term, $\rho \overline{u_i' u_j'}$, called the Reynolds stress, which is a symmetric tensor with six unknown values. These additional terms lead to a closure problem. Turbulence modelling is applied to close this new system of equations. Most RANS turbulence models use the Boussinesq Eddy Viscosity Hypothesis (Schmitt [2007]). The eddy viscosity hypothesis is based on the observation that in turbulent flows, momentum transfer is dominated by turbulent mixing in large energetic eddies (Blazek [2005]). In RANS momentum and energy equations, the Reynolds stresses are assumed to be equal to the product of the mean velocity strain rate and the isotropic eddy viscosity. Different turbulence models take various approaches to model this eddy viscosity as will be discussed below.

The $k - \varepsilon$ (Launder and Spalding [1974]) and the $k - \omega$ (Wilcox [2008]; Menter [1994]) two-equation eddy viscosity models are the two most commonly used RANS turbulence models. These models solve additional transport equations for turbulent kinetic energy k and the turbulence dissipation rate ε or the specific turbulence dissipation rate ω which also include history effects like convection and diffusion of turbulent kinetic energy. Another feature of these turbulence models is that the buffer region of the boundary layer is modelled using wall functions and is thus not simulated. The $k - \varepsilon$ model is extensively used for external flow problems because of its good performance and convergence characteristics. However, the $k - \varepsilon$ model struggles to accurately predict flow in adverse pressure gradients and separated flow. The $k - \omega$ model is very sensitive to free-stream flow and initial conditions, but performs well at predicting stalled flow behavior. Menter [1994]'s $k - \omega$ Shear Stress Transport (SST) model utilizes the advantages of both the $k - \varepsilon$ and the Wilcox [2008] $k - \omega$ models but using a blending function that activates the $k - \omega$ model in the near-wall region and blends gradually to the $k - \varepsilon$ model in the far-field. The result is a more robust and accurate turbulence model that performs well in a large range of applications. This model is also particularly suited for applications in wind energy because of large local regions of separated flow near the blades and more uniform flow in the far-field.

The Spalart and Allmaras [1992] turbulence model developed at Boeing models eddy viscosity using a transport equation for magnitude of vorticity, algebraic constants, and a characteristic exponential equation that drives eddy viscosity to zero upstream of the transition point. This model is capable of differentiating fluid behavior in the free-stream and the boundary layer, resulting in increased robustness

and versatility. However, the model has a tendency to produce too much vorticity due to the fact that the model is based on vorticity, thus causing problems in accurately predicting stalled flow behavior.

Another class of RANS turbulence models is the so-called Reynolds Stress Transport models (Launder et al. [1975]). These models do not invoke the eddy viscosity assumption, but model each component of the Reynolds stress tensor instead. This leads to six additional differential transport equations that need to be solved along with the original RANS equations, and in most cases, this turns out to be too computationally expensive. Additionally, the Reynolds Stress Tensor (RST) model is very sensitive to the type of flow that is being simulated.

Because it is common to have separated flow in the simulation of wind turbines, it becomes clear that the applicability of RANS to this area of application is often limited, and depends on the goals of the study, as reported by Réthoré [2009]. It has also been reported that RANS models are problematic in predicting the transition of boundary layers from laminar to turbulent which then leads to inaccurate performance predictions of wind turbines (Xu and Sankar [2000]). One workaround is to combine a boundary layer transition model to the turbulence model.

3.3 OTHER CFD METHODS

Large Eddy Simulation is another technique of flow simulation where large turbulent length scales are resolved and small dissipative length scales are modelled, as opposed to RANS where all length scales are modelled. This is achieved by using a low-pass filter on the Navier-Stokes equations which eliminates small scales of the flow (Germano et al. [1991]). The cut-off length is chosen to be in the inertial range of the turbulence energy cascade (Figure 3.7), and is also dependent on available computational resources and the type of flow. LES is an inherently unsteady method and because the large scales are resolved, LES is capable of simulating anisotropic turbulent flows dominated by large scale structures and turbulent mixing.
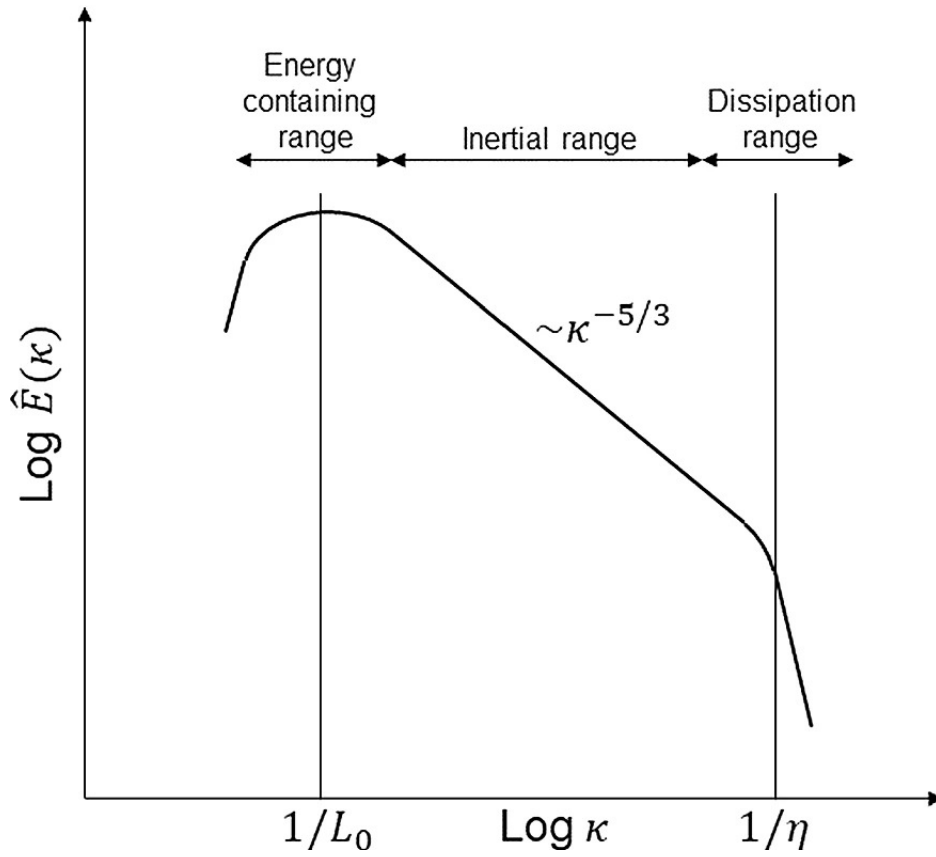
Figure 3.7: Kolmogorov Energy Spectrum showing the inertial range (Kalmár-Nagy and Bak [2019])

LES requires a much finer grid than RANS, and is therefore computationally more expensive. The resolved (filtered) velocity can be defined as a convolution operation

$$\overline{u_i}(x_i, t) = \int u_i(\xi_i, t) G_i(x_i - \xi_i, \Delta) d\xi_i \tag{3.36}$$

where $G_i(x_i - \xi_i, \Delta)$ is the convolution kernel and Δ is the filter width. The unresolved (sub-grid) velocity scales can then be defined as the difference between the flow velocity and the resolved velocity:

$$u_i'(x_i, t) = u_i(x_i, t) - \overline{u_i}(x_i, t) \tag{3.37}$$

The filtering operation on the Navier-Stokes equations produces an extra term, called the Sub Grid Scale (SGS) Stress and this term represents the effect of the small, unresolved scales on the resolved scales. Similar to RANS, there are several models that can be applied to compute the SGS term. The Smagorinsky [1963] model is one of the most popular LES sub-grid scale models and is based on the eddy viscosity hypothesis. There are several other models available, such as dynamic procedures and Variational Multiscale Models (Hughes et al. [2000]; Lilly [1992]). Because turbulence is inherently a 3D phenomenon, in cases of wall-bounded flows, refinements are needed in all dimensions, and this greatly increases the cost of wall-bounded LES (Piomelli and Balaras [2002]).

Attempts made to combine the relatively low costs of RANS and the ability of LES to capture complex flow has resulted in a hybrid model, called the Detached Eddy Simulation (Strelets [2001]). Detached Eddy Simulation (DES) uses RANS equations

in the near-wall region and couples this to LES in the regions away from the wall. If eddy viscosity models are used for the RANS and LES, then the change of eddy viscosity of LES and RANS can be easily matched using wall distance functions. There will, however, be a mismatch between the modelled Reynolds stresses in RANS and resolved stresses in LES at the RANS/LES interface (Piomelli and Balaras [2002]). This results in larger velocity gradients at this interface. Naturally, the computational cost of DES is in between that of RANS and LES, but also depends to some extent on the flow Reynolds number.

4 | PROBLEM DEFINITION AND SETUP

This chapter presents the geometry definition of the Wind Turbine Blade being studied, including the baseline blade and the modified winglet configurations and the set up of the problem on OpenFOAM and AWSM.

4.1 THE DANAERO LM 38.8M BLADE

This entire study is based on the LM38.8m Wind Turbine Blade used as a part of the DanAero project and the International Energy Agency (IEA) Task 29 Phase IV (Schepers et al. [2021]) whose main goal was to "enhance the level of knowledge in wind turbine aerodynamics and to develop, validate, and improve aerodynamic models for wind turbine design codes" (Schepers et al. [2021]). This was a large multinational cooperative study which resulted in a huge database of aerodynamic experimental and numerical data for the LM38.8m blade. This extensive availability of data was one of the primary reasons for choosing this blade as the baseline for this study, and the basis for modifications to generate winglet designs.

Figure 4.1: The LM38.8m Wind Turbine Blade

Experimental data from the Tjæreborg Wind Farm 2MW NM80 wind turbine and Wind Tunnel Tests from VELUX (DK), LM Glasfiber Low Speed Wind Tunnel (DK) and the TU Delft Low Speed Low Turbulence Wind Tunnel (Aagaard Madsen et al. [2010]) as well as CFD results (Schepers et al. [2021]) from the DanAero Database will be used for the Verification and Validation of the OpenFOAM CFD model that will be developed for this study and for the AWSM setup as well.

4.2 WINGLET DESIGNS

The main goal of this study is to assess the performance of AWSM for the case of winglets mounted on wind turbine blades by comparison to CFD results. For this reason, it was deemed unnecessary to develop optimized winglet designs for the blade, instead, simple un-optimized winglet designs were considered. A major consideration for this approach was the time-constraint this study was subject to. Three simple winglet designs were considered.

The first winglet configuration was a simple constant chord extension with a winglet span of 3% of the blade span with a cant angle of 0 degrees. The winglet was generated such that the total span of the blade-winglet configuration along the pitching axis was the same as the baseline blade. Figure 4.2 shows the Winglet Configuration 1 in comparison to the Baseline Blade.
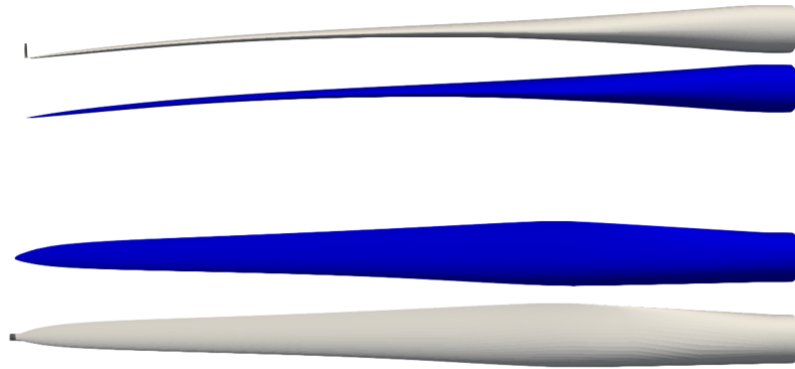
Figure 4.2: Winglet Configuration 1

The second winglet configuration is generated by bending the baseline blade in the downstream direction at 7% of the span from the end such that it is perpendicular to the pitching axis. This configuration preserves the curvilinear length of the baseline blade. Figure 4.3 shows the Winglet Configuration 2 in comparison to the Baseline Blade.
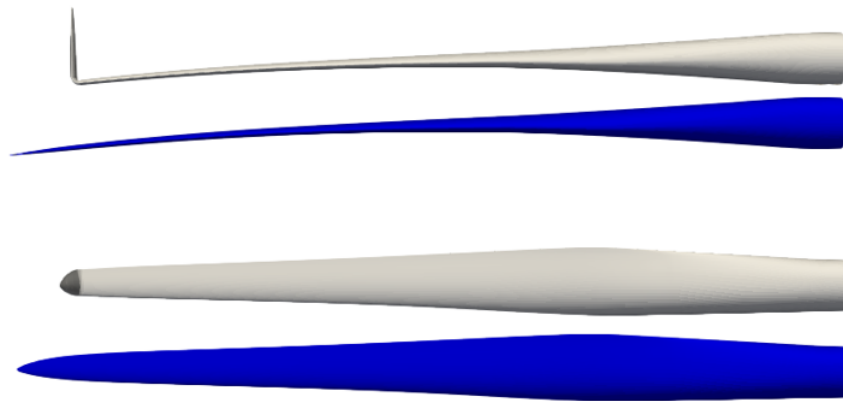
Figure 4.3: Winglet Configuration 2

The third winglet configuration is generated by bending the baseline blade in the downstream direction at 7% of the span from the end such that it is at 45 degrees to the pitching axis, and it is then scaled in the direction of the winglet span such that the span of the blade-winglet configuration in the pitching axis direction is the same as the span of the baseline design (rotor diameter is maintained).
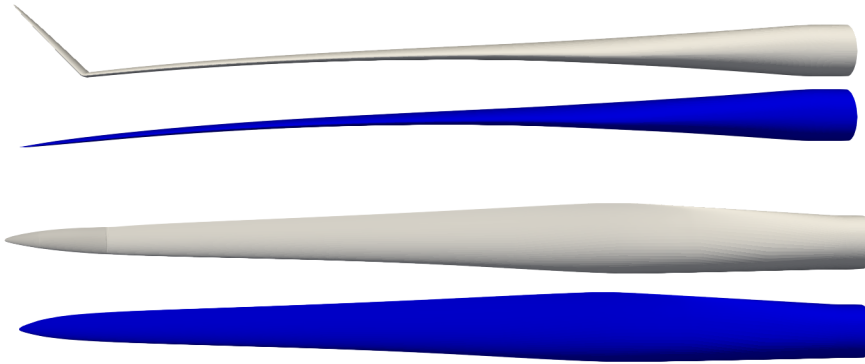
Figure 4.4: Winglet Configuration 3

The three winglet configurations were selected such that either the curvilinear length of the blade or the length of the blade along the pitching axis was similar to the baseline blade. These configurations also shift the operating point of the blades, so that different operating points can be studied for the same input conditions.

4.3 SETUP OF THE PROBLEM ON OPENFOAM

4.3.1 Mesh Generation

The Computer-Aided Design (CAD) model of the DanAero LM38.8m blade was available in the DanAero Database, and was used for the creating the OpenFOAM model. A 120° sector domain was generated using a single blade and by invoking symmetry arguments. The mesh was generated using the mesh generation tool Pointwise. As a trade-off between solution accuracy and time required for creating the mesh, a hybrid mesh topology was preferred.

The computational domain consists of three distinct sections: the far-field, the near-field, and the near-wall regions. A structured approach was adopted for the far-field discretization because it mainly consisted of regular geometry blocks composed of circular and annular sectors.
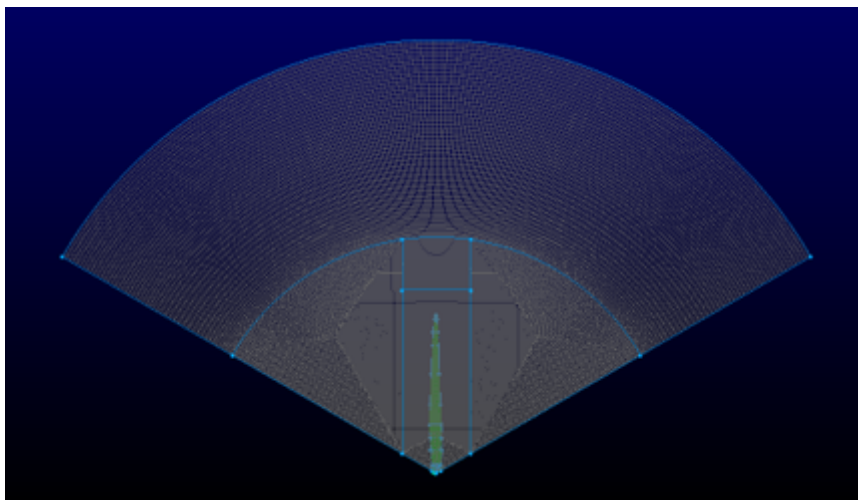
Figure 4.5: Structured Domain in the Far-Field

The near-field region was discretized using an unstructured approach due to the difficulty of merging the irregular boundaries of the near-wall region with the regular boundaries of the far-field region. Pointwise offers a hybrid meshing algorithm, called T-rex, which seamlessly blends the structured and unstructured regions using structured prismatic layers that slowly morph into an isotropic unstructured mesh. This helps prevent sudden changes in mesh size in between different sections.
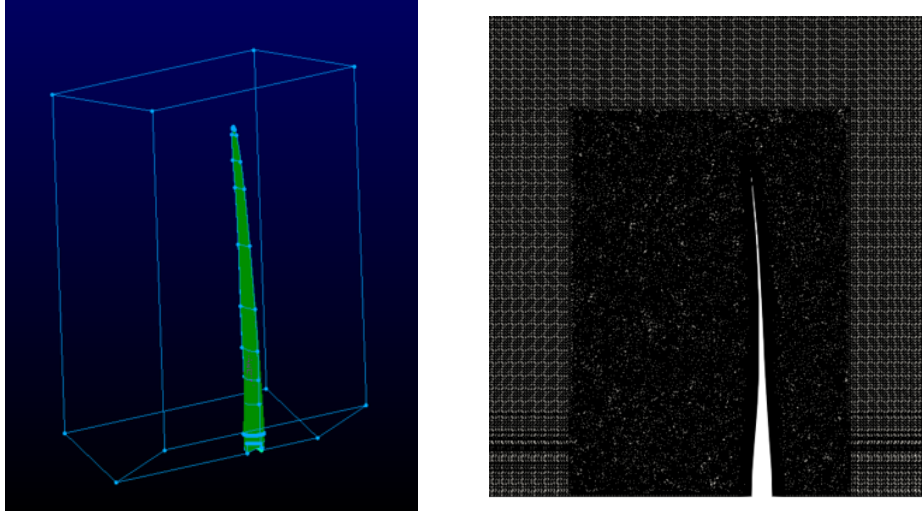
Figure 4.6: Unstructured Domain in the Near-Field

The near-wall region was discretized using a fully structured mesh in several sections along the span of the blade. This region was divided into several sections to allow individual control of near-wall spacing of the cells of each section. Because near-wall region of the blade sees large changes of velocity along the span of the blade as a result of its rotation, and because of the restriction on first cell height imposed by the turbulence model ($y+ \approx 1$), the required height of the first cell changes considerably over the span. By dividing the near-wall region into several sections along the span, this requirement for $y+ \approx 1$ was met over the entire span of the blade.
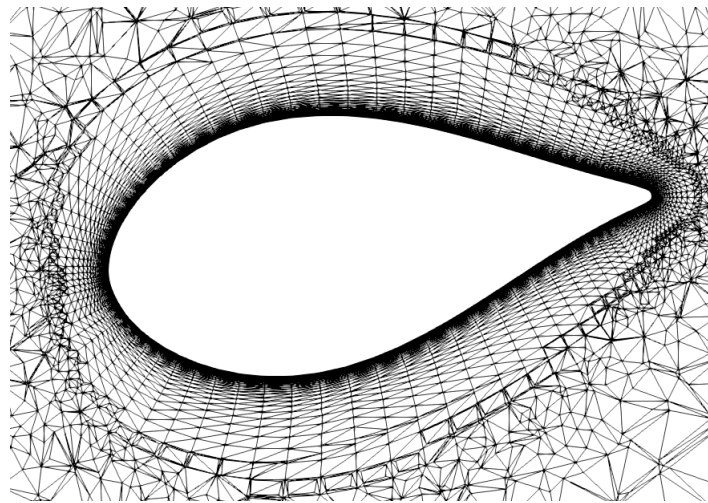
Figure 4.7: Structured Domain in the Near-Wall Region

Between these near-wall sections, a boundary condition of shared boundaries was imposed to ensure smooth change of cell size over the sections. In total, 25 structured prism layers were generated in the near-wall region, and this was added to by the T-rex algorithm in the near-field region.

Figure 4.8: Structured Surface Mesh on the Blade

4.3.2 OpenFOAM Solver Setup

A Moving Reference Frame (MRF) approach was chosen for this problem. With the MRF, the problem gets transformed into a steady state problem, with body forces introduced in the MRF domain to account for the angular velocity of blade.

This was set up in OpenFOAM by first defining a TopoSet in the TopoSetDict file specifying the rotating and non-rotating patches. The angular velocity of the blade was defined in the MRFProperties dictionary based on the specific operating case.

Turbulent Eddy Viscosity is modelled using the $k - \omega$ SST turbulence model. The choice of this turbulence model for the simulation of wind turbine blades is supported extensively in literature, with studies by Gaunaa and Johansen [2007]; Johansen and Sørensen [2006]; Ferrer and Munduate [2007], among others using the turbulence model for cases similar to the present study.

The simpleFOAM solver is used, which solves the steady state incompressible flow equations, and uses the Semi-Implicit Method for Pressure-Linked Equations (SIMPLE) algorithm to enforce pressure-velocity coupling. Additional dictionaries are defined within the system folder to extract solution residuals and to calculate blade forces and wall shear stress.

4.4 AWSM SETUP

Input for AWSM is specified using text files. The DanAero LM38.8m blade is defined in AWSM using the AeroProps table, which is a table containing geometric information about the blade such as the radial location of the different sections of the blade (zB), the local chord at each section, the local twist, airfoil thickness, and the location of the quarter chord point of each section (xB and yB). All required data is available in the DanAero Database. The winglet geometry is defined by modifying xB and yB.

The Lifting Line Method does not physically model the local airfoil geometry, but instead uses airfoil polars to compute the circulation the airfoil at that section would generate. These airfoil polars are supplied as separate input files and included in the main input file. Additionally, depending on how the airfoil polars were generated, there is an option to apply a 3D correction to the polars to account for the three-dimensional behaviour of the flow over the blade. Three dynamic stall

models are available to account for the dynamic behaviour of the flow.

The input file also specifies the number of wake points that are simulated, i.e. the length of the wake. The number of wake points are set such that the length of the wake is three times the diameter of the rotor. A separate input file defines special parameters such as the controls for printing output files, numerical controls, and the size of the vortex core region.

Time step size is chosen to correspond to $10°$ rotation of the blade and the end time is chosen such that the end position of the blade is the same as the start position of the blade and long enough to ensure the solution has fully converged.

(a) Time History of Coefficients of Power and Thrust

(b) Root Mean Square Deviation
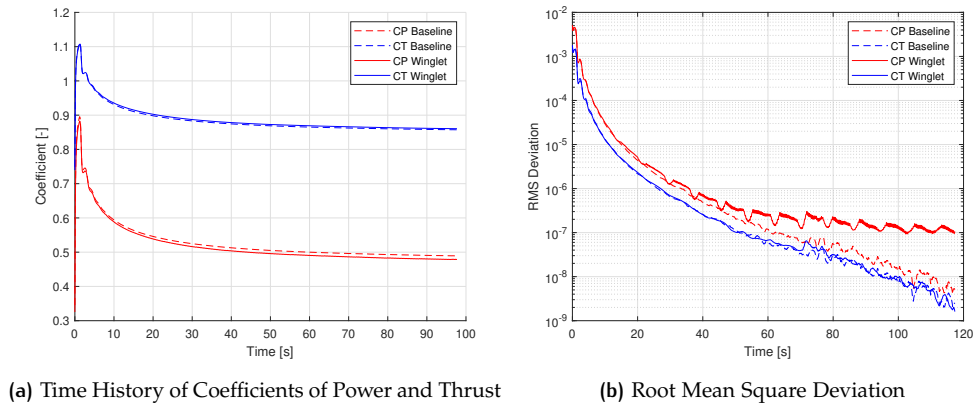
Figure 4.9: Convergence of AWSM Simulations
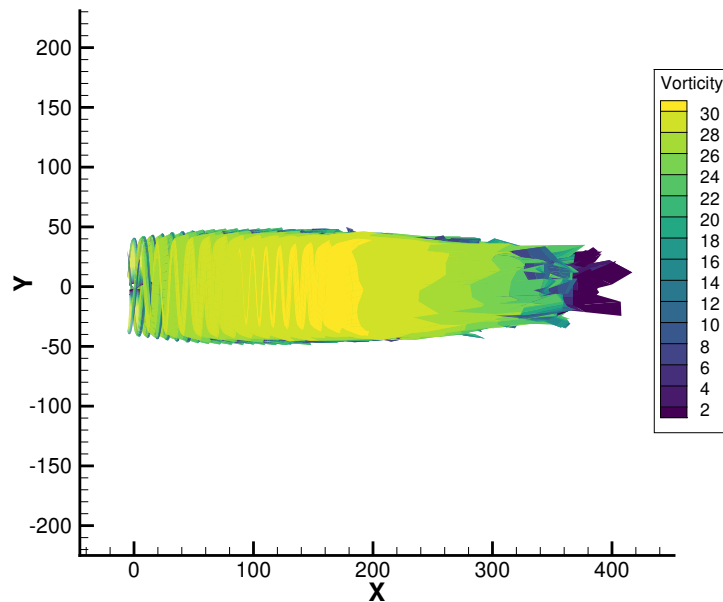
Figure 4.10: Evolution of the Wake for the Baseline Case

Figure 4.9a shows the convergence history of the power and thrust coefficients calculated by AWSM for both the baseline case and one of the cases with a winglet. As mentioned previously, the simulation was run for the time it takes for the wake to convect a little more than three times the diameter of the rotor downstream

(Figure 4.10). In Figure 4.9b, the windowed Root mean square deviation of the solution is plotted. The RMS Deviation is defined as

$$RMSD_j = \sqrt{\frac{\sum_{i=0}^{n}(x_i - \bar{x})^2}{n-1}} \tag{4.1}$$

and is the moving root mean square deviation of the solution with a window size of n. Here, a window size of $n = 20$ was chosen. A threshold value of $RMSD = 1e - 06$ was chosen, and the rms deviation for all variables has dropped below the threshold within the chosen simulation time.

5 | VERIFICATION AND VALIDATION

5.1 GRID INDEPENDENCE STUDY

The method of Grid Independence Study used for this project is based on the method proposed by Roache (Roache [1998]). The method uses Richardson Extrapolation (see Roache and Knupp [1993]) to examine the spatial convergence of a simulation by performing two or more simulations on progressively finer grids.

The first step is to generate a *fine* grid, based on the available time and computational resources and then generating coarser grids by removing alternate grid points in every direction. Several levels of coarser grids can be generated, however, it is common practice to perform the grid independence study on three levels of coarsening. It is also possible to coarsen the grid by non-integer ratios, but this will require generation of new grids and redistribution of the new grid points along the geometry.

The order of grid convergence is determined by the behaviour of the solution error expressed as the difference between the discrete solution and the exact solution

$$E = f(h) - f_{exact} = Ch^p + H.O.T \qquad (5.1)$$

where C is a constant, h is a measure of grid spacing, and p is the order of convergence. The order of convergence of the solution will, in practice, be lower than the theoretical order of convergence established by the numerical algorithm that the CFD code uses. This may be because of several reasons, such as, applications of boundary conditions, use of approximate models, etc.

From Equation 5.1, by neglecting the higher order terms and taking the logarithm on both sides, we get

$$log(E) = log(C) + p log(h) \qquad (5.2)$$

Here we can observe that the order of convergence p is the slope of the graph of $log(E)$ vs $log(h)$. This data can be obtained from successively refined CFD solutions and the actual order of convergence can be computed. If a constant refinement ratio is used, the equation can be simplified as

$$p = ln\left(\frac{f_3 - f_2}{f_2 - f_1}\right)/ln(r) \qquad (5.3)$$

where r is the refinement ratio and f is the CFD solution for different grids.

The grid needs to be sufficiently refined such that the solution is in the asymptotic range of convergence in order to assess the accuracy of the code and calculations. This asymptotic range of convergence is obtained when the grid spacing is such that error E for different grid spacings h result in a constant value for C

$$C = E/h^p \qquad (5.4)$$

A higher-order estimate of the continuum value (i.e. at zero grid spacing) can be obtained using Richardson Extrapolation using a series of discrete values. In the most general form, the quantity f yielded by a simulation can be expressed by a series expansion

$$f = f_{h=0} + g_1 h + g_2 h^2 + g_3 h^3 + \dots \qquad (5.5)$$

where h is the grid spacing and g_1, g_2, g_3, etc. are functions independent of the grid spacing. A second-order calculation of $f_{h=0}$ using the generalized Richardson extrapolation of values obtained using two different grid spacings h_1 and h_2 is given as

$$f_{h=0} \approx f_1 + \frac{f_1 - f_2}{r^2 - 1} \qquad (5.6)$$

This can easily be generalized to a $p - th$ order method

$$f_{h=0} \approx f_1 + \frac{f_1 - f_2}{r^p - 1} \qquad (5.7)$$

To provide a consistent manner in reporting the results of the grid convergence studies Roache [1998, 1994] suggests a parameter called the Grid Convergence Index (GCI). The GCI is a measure of the percentage the computed value is away from the asymptotic numerical value. It indicates how much the solution would change with further refinement of the grid. The GCI is defined as

$$GCI = \frac{\mathcal{F}_s |\varepsilon|}{(r^p - 1)} \qquad (5.8)$$

where $\mathcal{F}_s$ is the factor of safety and ε is the relative error between the solution of two grids. The recommended value for the factor of safety is $\mathcal{F}_s = 3.0$ for comparisons between two grids and $\mathcal{F}_s = 1.25$ for comparisons between three or more grids.

It is important for the results of each grid to lie in the asymptotic region of convergence. If the solutions are indeed in the asymptotic region of convergence, the following relation should hold

$$\frac{GCI_{2,3}}{r_p GCI_{1,2}} \approx 1 \qquad (5.9)$$

For this project, the total power and total thrust on the blade will be used to conduct the grid independence study. The information on the grids is presented in Table 5.1

Grid	Normalized Grid Spacing	Power (kW)	Thrust (kN)
Fine (1)	1	306.296	97.200
Medium (2)	2	302.254	96.680
Coarse (3)	4	289.179	95.427

Table 5.1: Grid Details

A constant grid refinement ratio of $r = \sqrt{2}$ was used for generating the grids. Because the grid independence study is performed using comparisons between three grids, the factor of safety is taken as $\mathcal{F}_s = 1.25$ as recommended. Using the equations discussed above, the results of the grid independence study are tabulated in Table 5.2

	Power	Thrust
Order of Convergence	3.387	2.537
Richardson Extrapolation $f_{h=0}$	308.105	97.569
$GCI_{2,3}(\%)$	2.42	1.15
$GCI_{1,2}(\%)$	0.738	0.474
Asymptotic Check	$1.013 \approx 1$	$1.005 \approx 1$

Table 5.2: Grid Independence Study Results

It is evident from Table 5.2 that the solutions of all the grids obey Equation 5.4 and thus lie in the asymptotic region of convergence. For further simulations, the Medium grid will be used in order to strike a balance between computational costs and accuracy of results.

Figure 5.1 shows the behaviour of Power and Thrust on the blade for different grids and the predicted value for the same at zero grid spacing (using Richardson Extrapolation).
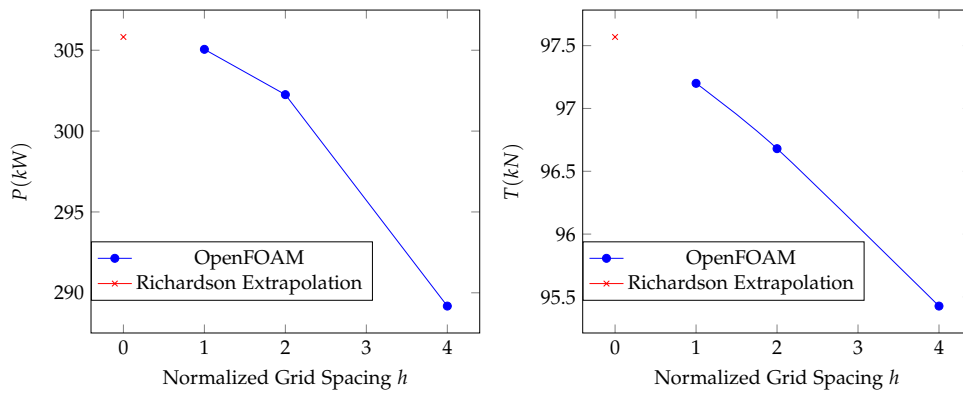

**Figure 5.1:** Grid Convergence Results

5.2 BASELINE DANAERO BLADE

In this section, the OpenFOAM model of the unmodified DanAero blade is verified and validated against previously validated CFD data from EllipSys3D for the same operating conditions.

The EllipSys3D study was conducted as a part of the IEA Task 29 Phase IV of the DanAero experiments. The study involved comparison of results from experiments as well as with a variety of aerodynamic models including Blade Element Momentum (BEM) methods and Free Vortex Wake Lifting-Line (FVWLL) methods. The case setup details are presented in Table 5.3. The comparison of Coefficient of Pressure (Cp) distribution at different radial locations with the present OpenFOAM model are shown in Figure 5.2.

Wind Speed	$6.1 m/s$
Rotor Speed	$12.3 RPM$
Yaw Angle	$0°$
Air Density	$1.231 kg/m^3$
Turbulence Model	$\kappa - \omega$ SST

Table 5.3: OpenFOAM Case Setup
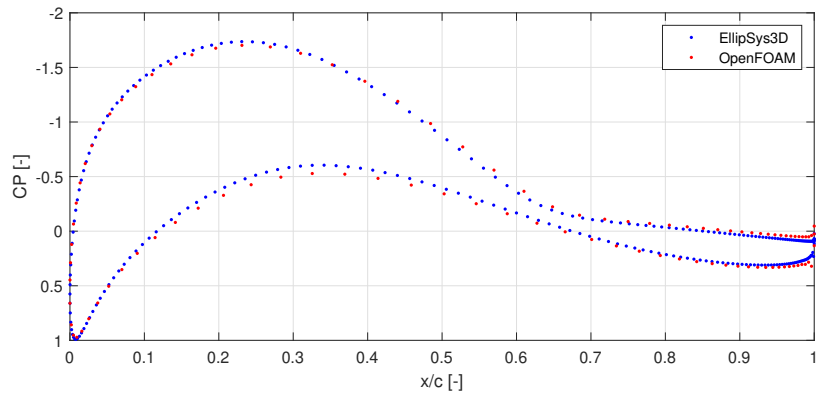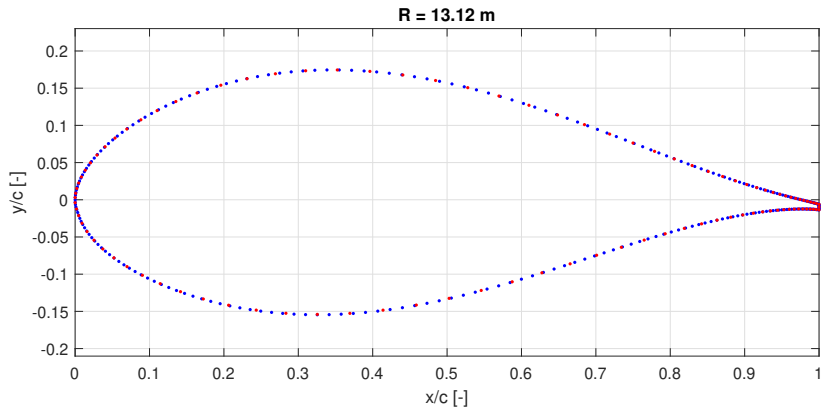
(a) Coefficient of Pressure Comparison at $R = 13.12m$
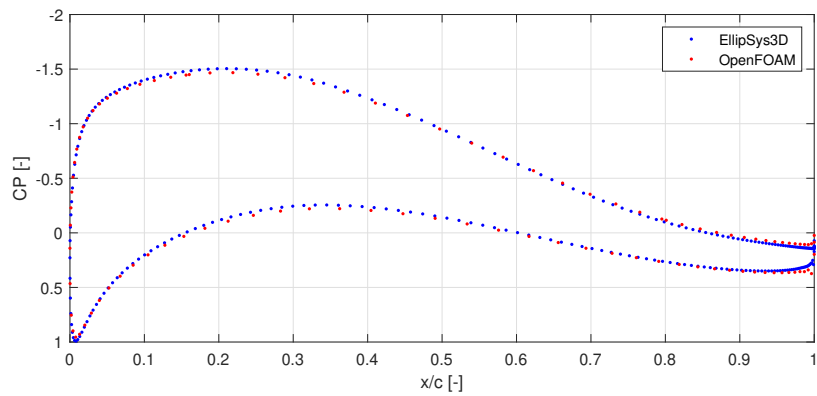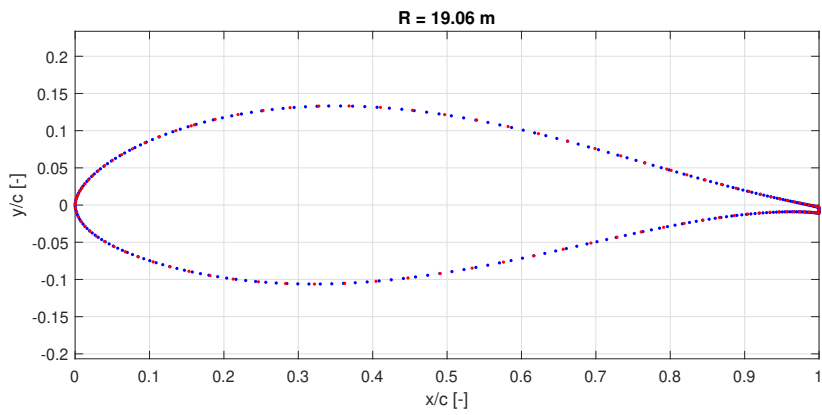
(b) Coefficient of Pressure Comparison at $R = 19.06m$
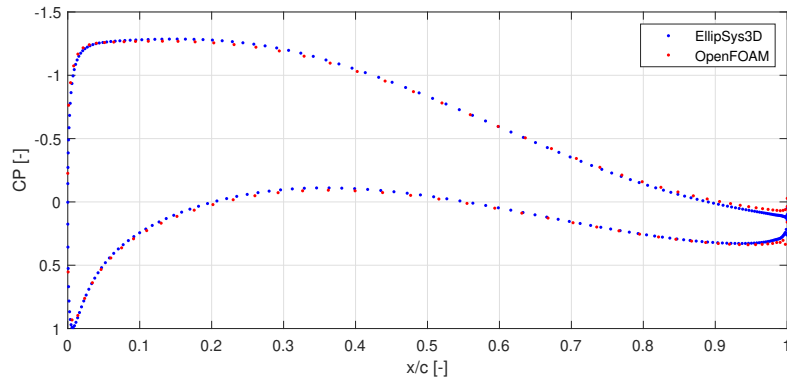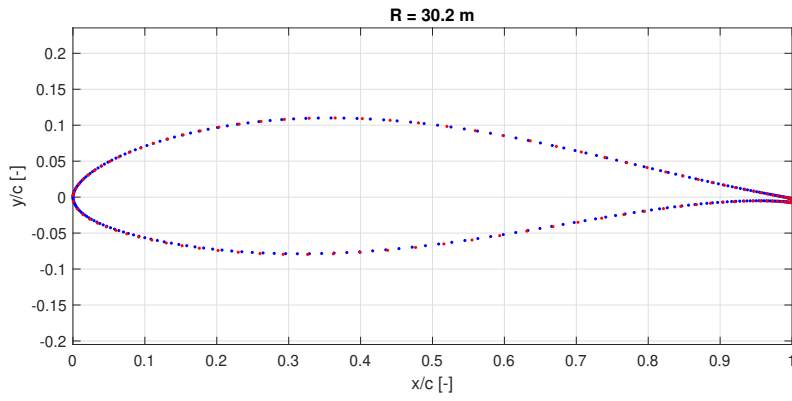
(c) Coefficient of Pressure Comparison at $R = 30.20m$
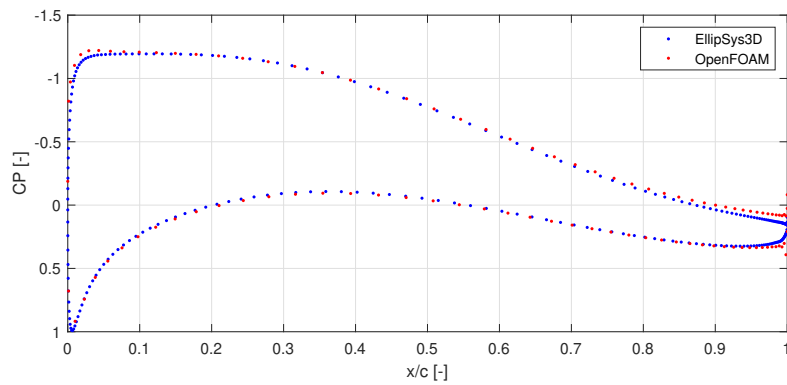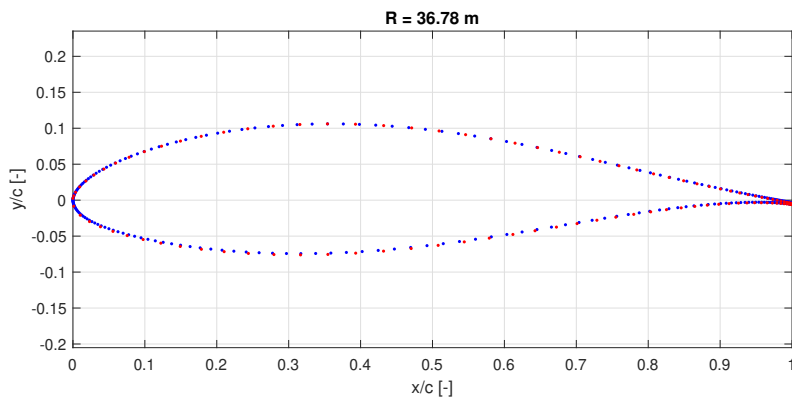
(d) Coefficient of Pressure Comparison at $R = 36.78m$

Figure 5.2: Comparison of Cp between EllipSys3D and OpenFOAM

The OpenFOAM simulation data was post-processed using a MATLAB script and Paraview. The MATLAB script modifies a skeleton Paraview Macro file with user specified inputs such as simulation directory address, radial station, and time steps. The script then runs Paraview in the background using this macro file and outputs a data file containing formatted geometry, pressure, and wall shear stress data which is then used to compute the coefficients of pressure and skin friction as well as the axial and tangential forces and compares it with available data for verification and validation.
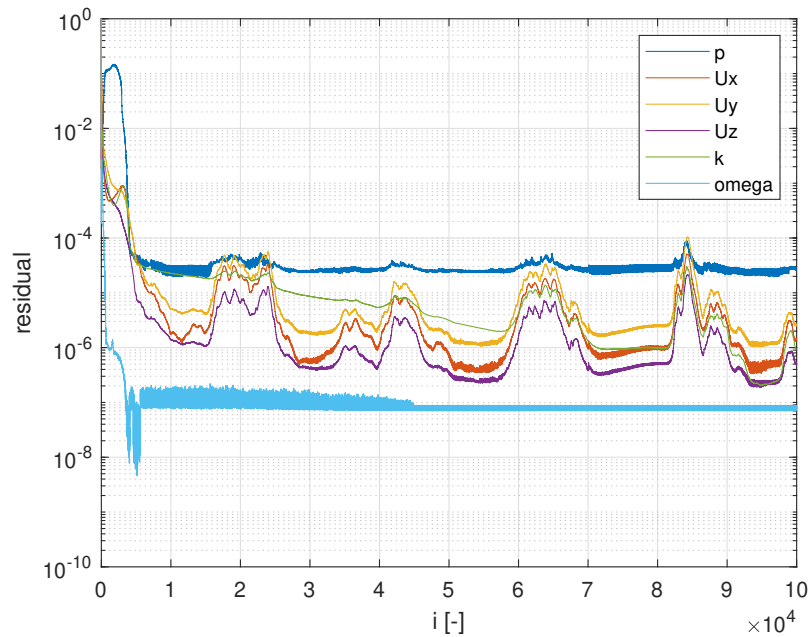
Figure 5.3: Residuals for the Baseline Simulation

The residuals from a simulation are plotted in Figure 5.3. It is observed that after about 25000 iterations, the residuals do not drop further but exhibit an oscillatory behaviour. This may be because of the unsteady nature of massively separated flow near the cylindrical hub region of the blade (see Figure 5.4).

(a) Suction Side

(b) Pressure Side

Figure 5.4: Line Integral Convolution of Wall Shear Stress showing massively separated flow at the root section of the blade

For a steady state simulation in this case, it may not be possible to obtain a fully converged solution, but it is sufficient if the solution around the lift generating parts of the blades is converged. To check the convergence of the solution in these regions, the evolution of the coefficient of pressure (Cp) and coefficient of friction (Cf) at four radial locations are studied as the simulation progresses. The observations are plotted in Figure 5.5. From these plots, it is evident that both the Cp and Cf at each radial location do not show any large variations, and thus the solution in this region can be assumed to be converged sufficiently.
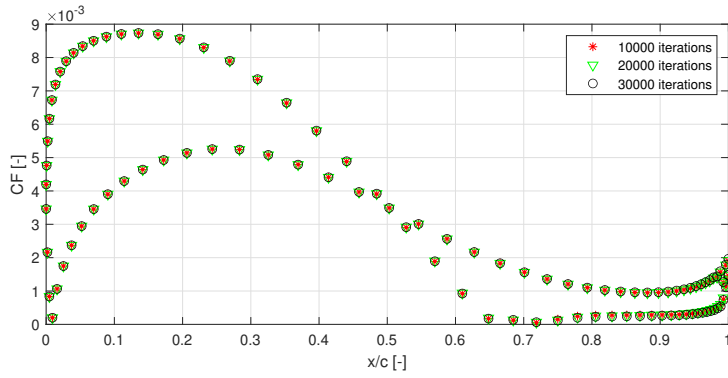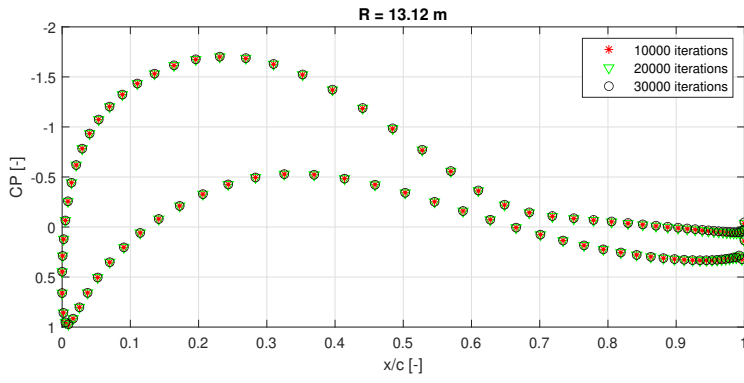
(a) Intermediate solutions at $R = 13.12m$

(b) Intermediate solutions at $R = 19.06m$

(c) Intermediate solutions at $R = 30.20m$
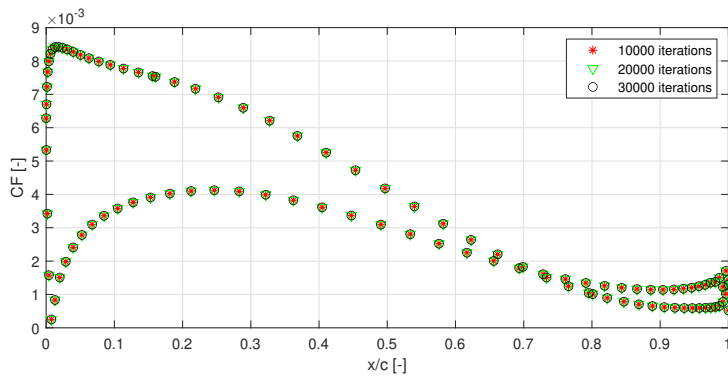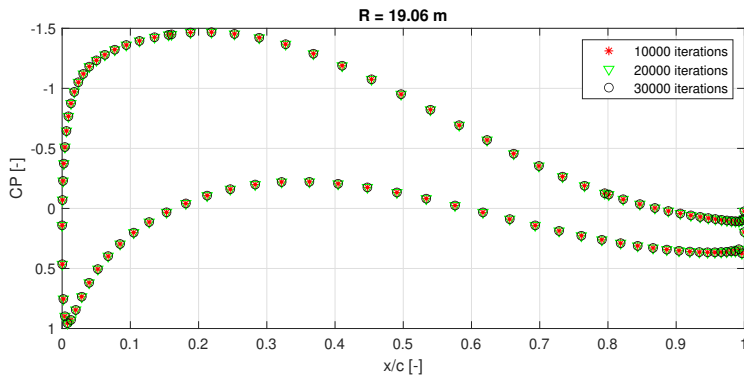
(d) Intermediate solutions at $R = 36.78m$
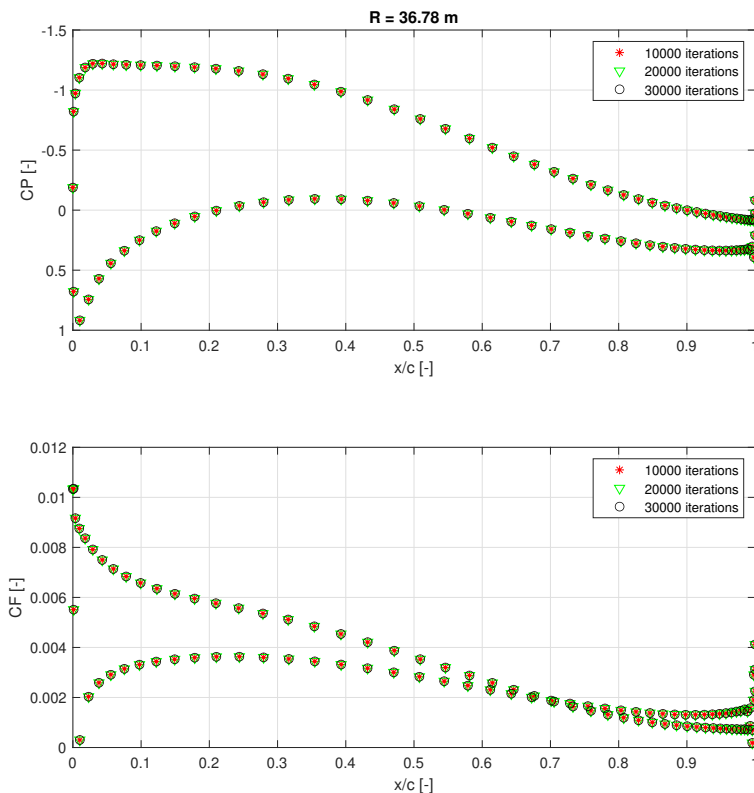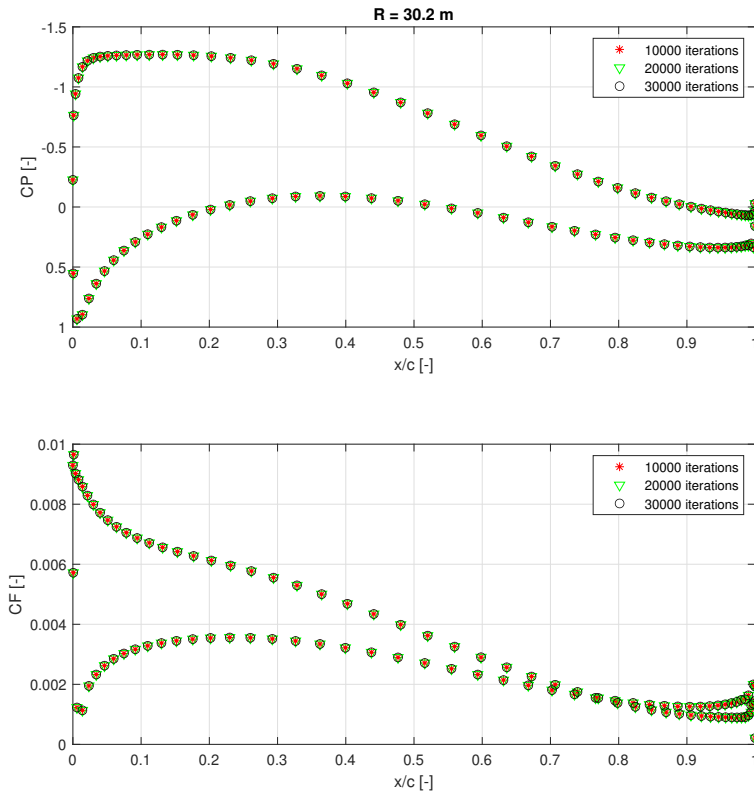
Figure 5.5: Convergence

Figure 5.6 shows the comparison of the normal and tangential forces with respect to the rotor plane. Both OpenFOAM results and AWSM results for the baseline de-

sign are compared to the experimental data and simulation data (using EllipSys3D) obtained from the DanAero Database.

In general, OpenFOAM predictions of the normal force ($F_{n,r}$) are very close to the predictions from EllipSys3D obtained from the DanAero Database and tangential forces show good agreement with reference values towards the outboard of the blade.

(a) Normal Force

(b) Tangential Force
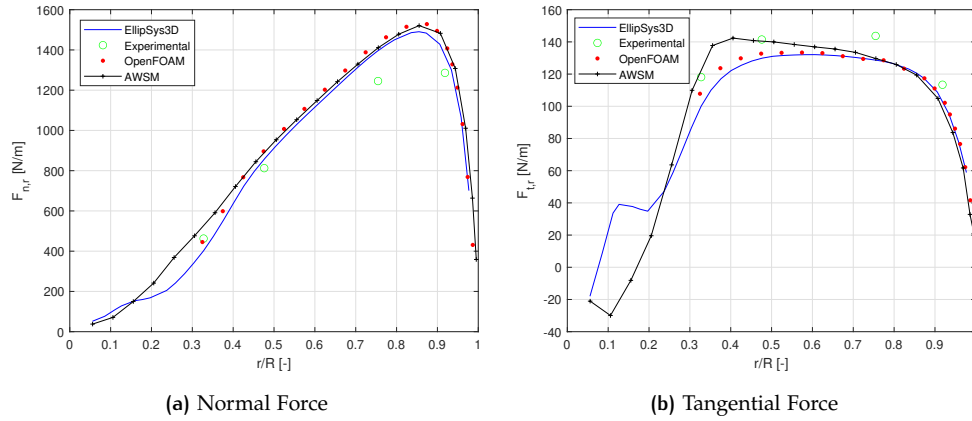
Figure 5.6: Integrated Forces wrt the Rotor Plane

5.3 COMPUTATION OF CIRCULATION FROM OPENFOAM DATA

Circulation is defined as the negative of the line integral of velocity around a closed curve in the flow field (Anderson Jr [2010]). Mathematically, circulation is denoted by Γ and is given by

$$\Gamma \equiv - \oint_C V \cdot ds \qquad (5.10)$$

where C is an arbitrary closed loop in the flow field. This idea of computation of circulation is presented in Figure 5.7.
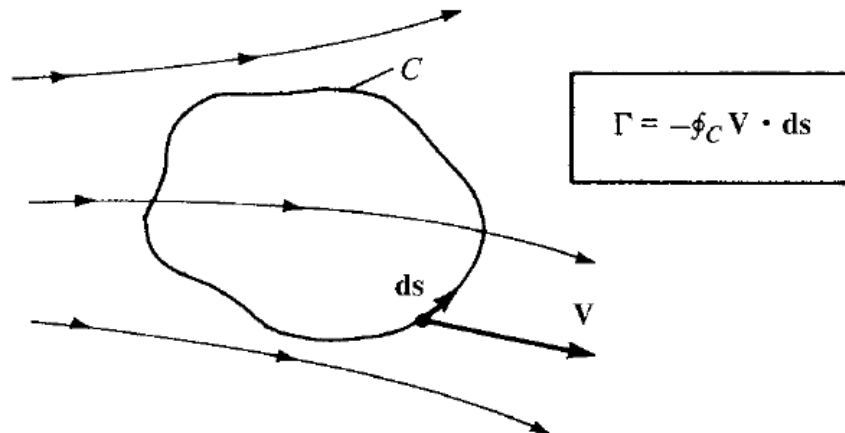
Figure 5.7: Definition of Circulation (Anderson Jr [2010])

Since AWSM and the Lifting Line Theory calculate the circulation that would be produced by the airfoils at each element, comparing the circulation distribution over the blade predicted by AWSM with circulation calculated using CFD data would be a means to validate the performance of the Lifting Line code.

Circulation is computed from the OpenFOAM data by means of a post-processing script developed on MATLAB. The MATLAB script uses a pre-defined ParaView macro file to write a series of macro files that are programmed to extract velocity data on planes at different radial locations (Figure 5.8).
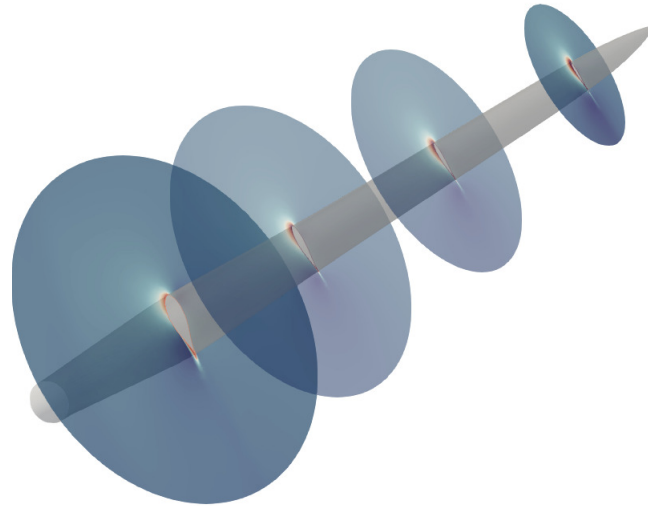
Figure 5.8: Cross-sectional Velocity Data extracted from Paraview for Computation of Circulation

The script then executes these macro files on ParaView using the command line interface and extracts velocity from the OpenFOAM simulation and stores it in text files. Next, the data is imported into MATLAB and conditioned to be efficiently used. An ellipse is chosen as the integration loop with the major axis oriented along the chord at each section. The ellipse parameters are fine tuned for each radial location. The script defines points along the ellpise and interpolates velocities from the flow field on to the ellipse (Figure 5.9).

(a) Domain Cross-section at $r/R = 0.46$

(b) Domain Cross-section at $r/R = 0.77$
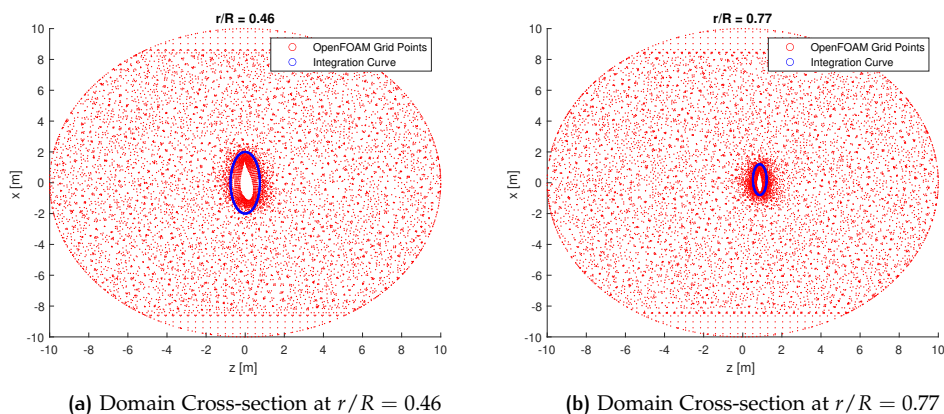
Figure 5.9: Integration Curves for the Computation of Circulation

Then, a trapezoidal numerical integration is performed over the ellipse to compute circulation. The results from this computation are presented in Figure 5.10.
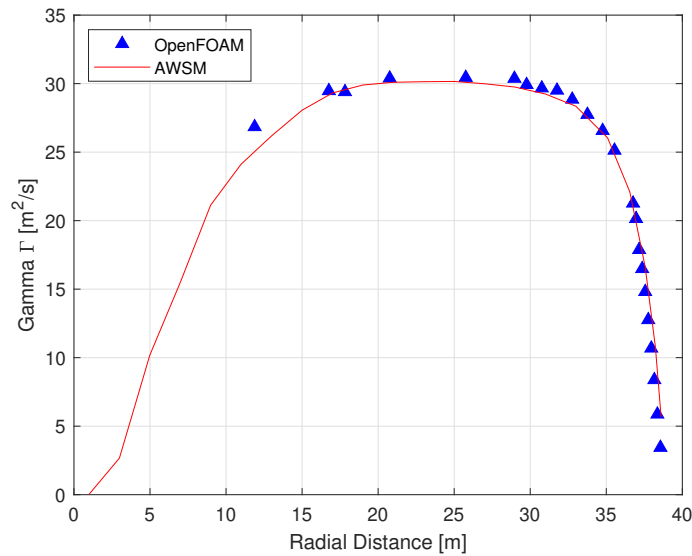
Figure 5.10: Circulation Distribution over the Blade

The circulation computed from the OpenFOAM dataset shows close agreement with the circulation computed from the vortex method, AWSM. The cases with winglets will be processed in a similar way, extracting data from OpenFOAM in planes aligned with the local airfoil sections. This is consistent with the circulation computed by AWSM in planes perpendicular to the local bound vortex element.

5.4 COMPUTATION OF AXIAL INDUCTION FACTOR AND THE TIP LOSS FACTOR FROM OPENFOAM DATA

The Tip Loss Factor, expressed in terms of the axial induction, can be written as

$$TLF = \frac{\overline{a}}{a_B} \tag{5.11}$$

where $\overline{a}$ is the azimuthally averaged axial induction and a_B is the axial induction on the blade. The definition of axial induction on the blade in CFD is not possible because of the physical presence of the blade, making it impossible to compute the induced velocity field. This is not a problem for the lifting line code because it is possible to compute the induced velocity field around each bound vortex element, which replaces the physical blade section. Methods to estimate the blade induction from CFD will be discussed in the present section, as well as methods to compute the azimuthally averaged axial induction distribution.

The first method to compute axial induction is adopted from a method originally proposed by Johansen and Sørensen [2004]. The simplified form of this method involves extracting velocity data from a series of planes perpendicular to the rotor axis set a different distances upstream and downstream of the rotor (Figure 5.11).
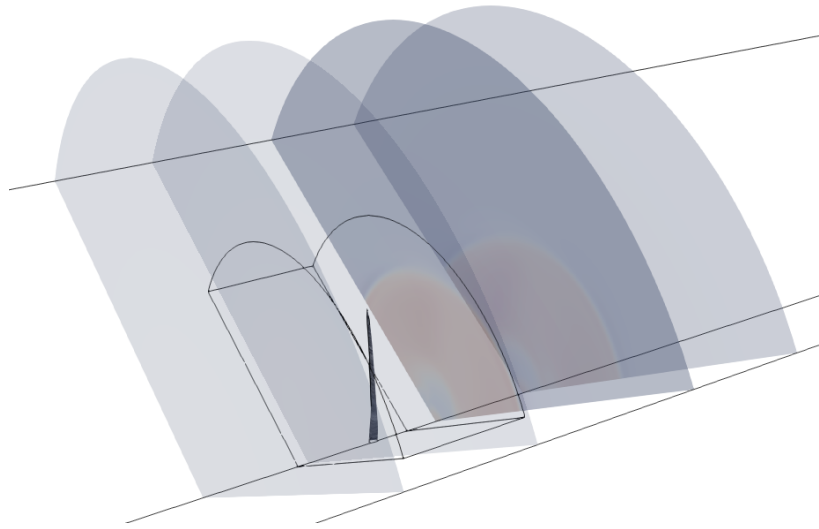
Figure 5.11: Data extracted from planes perpendicular to rotor axis

These planes are then split into several annular sections and the velocity field on each plane is averaged over each annular section. This averaged velocity field is used to compute the local axial induction using the relation

$$a = \frac{U_\infty - U_{local,avg}}{U_\infty} \qquad (5.12)$$

To compute the axial induction at the rotor plane (or a the location of the blade for non-straight blades), interpolation is performed for each annular section to obtain the azimuthally averaged axial induction distribution over the span of the blade.

(a) $r/R = 0.33$

(b) $r/R = 0.55$

(c) $r/R = 0.90$
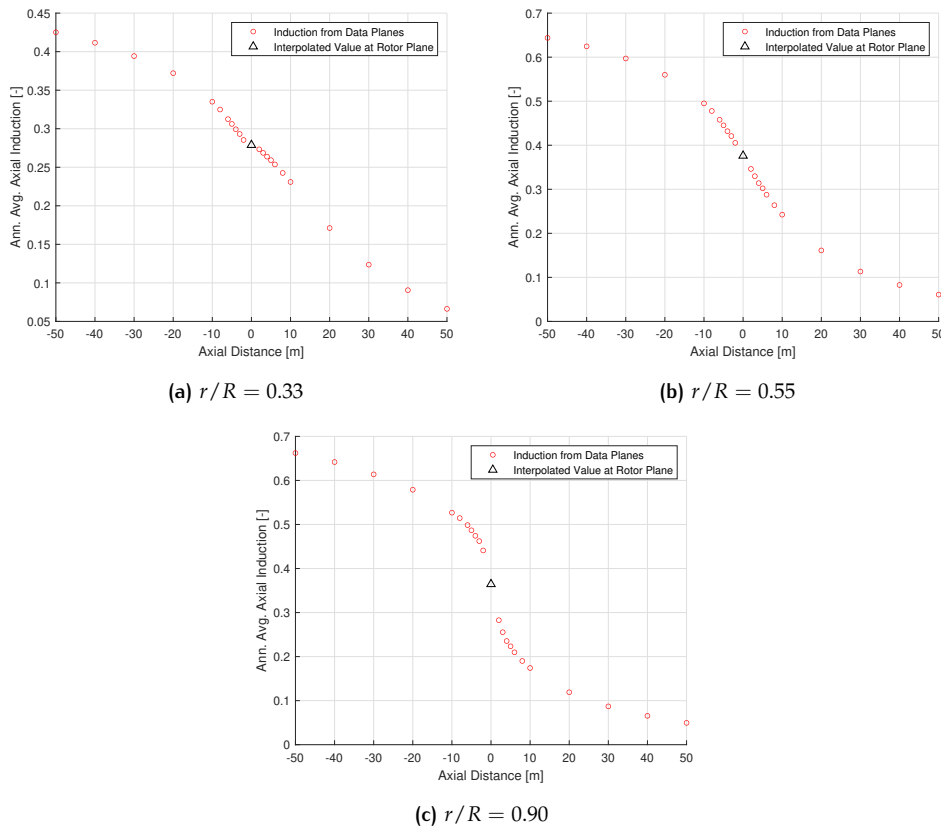
Figure 5.12: Azimuthally Averaged Axial Induction and Interpolated Values at Rotor Plane

To compute blade induction, Branlard [2011] suggests three methods, centered around the idea of extracting velocity data from annular sectors upstream and downstream of the blade (Figure 5.13).

Circular sectors

Rectangular sectors

Circular sectors of different central angle
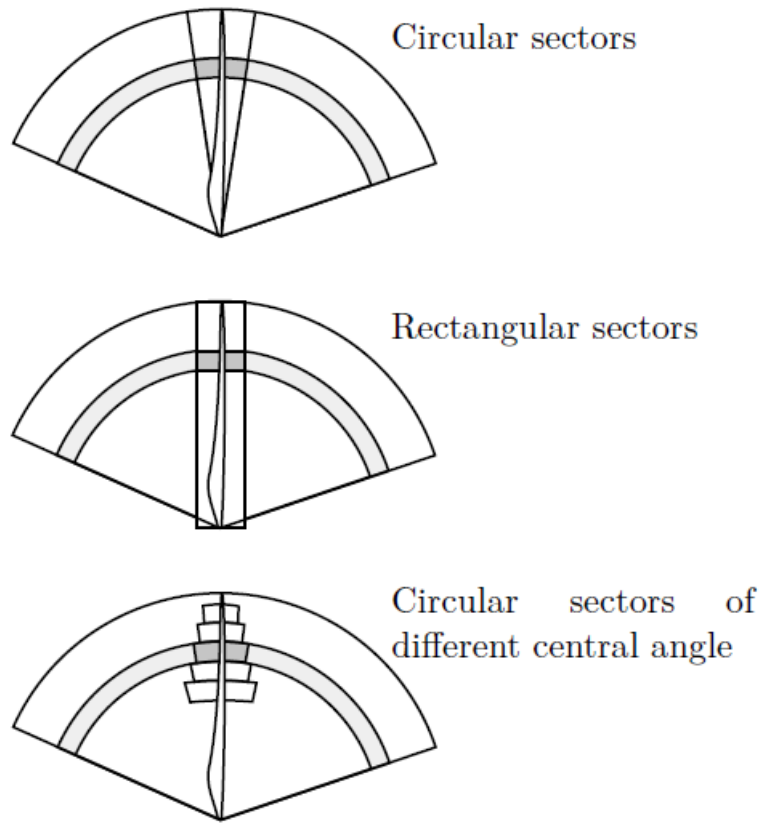
Figure 5.13: Methods to Compute Average Velocity near the Blade (Branlard [2011])

The circular sectors method is very simple to implement, but the annular sectors near the hub become very small and fail to account for the whole size of the blade at that location, and covers a much larger area near the tip. This drawback is overcome by the rectangular sectors method by setting the size of the rectangle as wide as the widest section of the blade, but cutting rectangular sectors breaks the azimuthal structure of the problem. The third method overcomes all the previously mentioned drawbacks by selecting the local circular sector size as a proportion of the local chord. This is done using the relation

$$\theta_i r_i = k c_i \qquad (5.13)$$

where θ_i is the central angle of the sector, r_i is the radial distance from the rotor axis, c_i is the local chord, and k is a parameter that controls the size of the sector. This method is harder to implement, but offers flexibility in choice of the sector size, and as a result yields superior results. As suggested by Branlard [2011], choosing a value of $k = 3$ gives good results. As the value of k increases, the result tends towards the azimuthally averaged values, as expected. The sensitivity of the calculation of axial induction to the parameter k is presented in Figure 5.14.
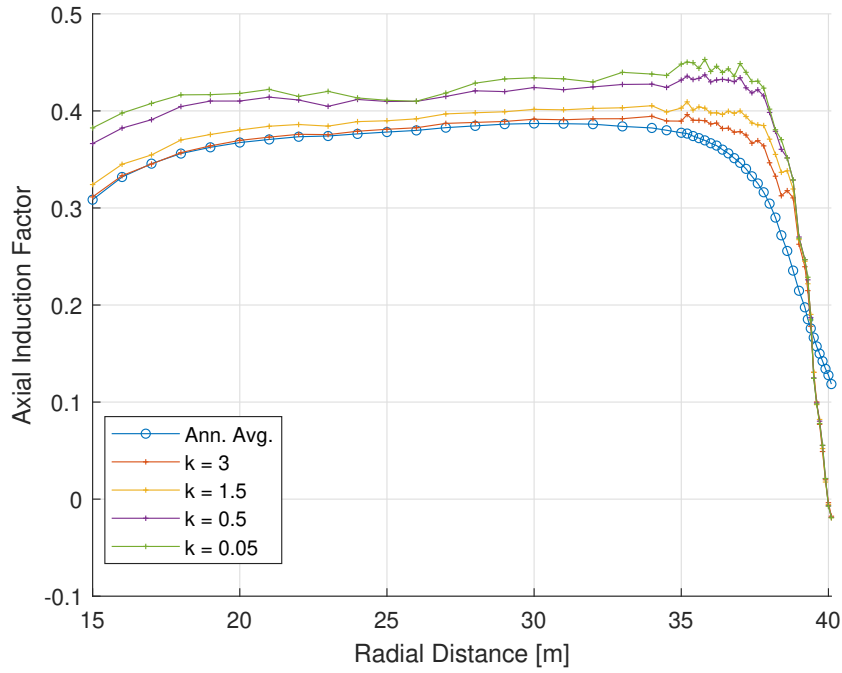
Figure 5.14: Sensitivity of Axial Induction to the Parameter k

It must be noted that small oscillations in the axial induction are observed near the tip regions. These oscillations are thought to be because of the relatively small chord at the tip of the blade, leading to very small annular sectors. Because of the small number of velocity points that are averaged in these windows, strong velocity gradients nears the tip are not sufficiently smoothed out by the averaging process.

(a) Blade and Azimuthally Averaged Axial Induction
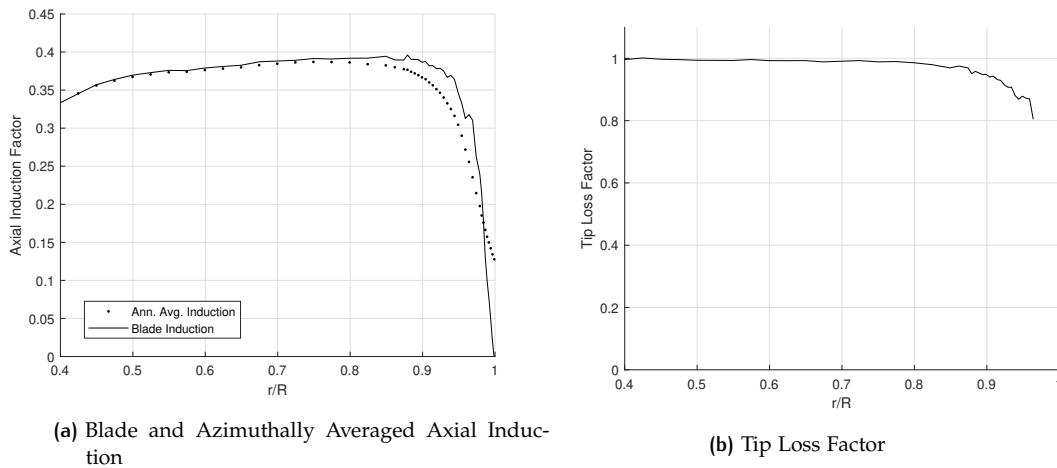
(b) Tip Loss Factor

Figure 5.15: Axial Induction and Tip Loss Factor for the Baseline Case

Figure 5.15 shows the Axial Induction and Tip Loss Factor for the Baseline Case computed using the methods mentioned in this chapter. The oscillations near the tip region of the blade are a minor drawback of this method, but shows the expected trend at in axial induction and the tip loss factor regardless.

6 | RESULTS AND DISCUSSION

This chapter presents the results from AWSM and OpenFOAM for different operating conditions of three different winglet configurations. The results are critically compared and attempts are made to explain the differences in predictions of the two methods.

6.1 WINGLET 1

The first case studied after the validation of the CFD model on OpenFOAM was the Winglet configuration 1, featuring a constant chord extension of the blade tip, keeping the total rotor radius unchanged. The case was simulated at a freestream wind velocity of $U_0 = 6.1m/s$ at a rotor speed of $12.3RPM$; the same operating conditions as the baseline DanAero LM 38.8m blade. The winglet geometry is presented in Figure 6.1 for ready reference.

Figure 6.1: Winglet Configuration 1 Geometry

Figure 6.2 presents the normal force and the tangential force predictions of Open-FOAM and AWSM in the rotor plane. The curvilinear distance along the blade has been normalized by the rotor radius $R = 40.04m$. Normal force predictions of AWSM are in good agreement with OpenFOAM predictions over most of the blade span, similar to the observations made with the baseline blade. Closer to the hub of the blade, the difference in predictions increases, with OpenFOAM results being slightly lower than those obtained from AWSM. As previously pointed out in Chapter 5, the reason for this disagreement is because of the use of transitional polars in AWSM, and also because of the fact that the solution fails to fully converge near the hub in OpenFOAM due to the highly unsteady nature of separated flow. This effect is more pronounced in the plots for the tangential forces. Drag has a large component in the tangential direction, and hence plays a large part in the prediction of tangential forces. Because AWSM uses transitional polars, the coefficient of drag of the airfoils is lower compared to fully-turbulent polars, and therefore, a larger tangential force distribution is expected in the results of AWSM. This is clearly visible in Figure 6.2b. Since the purpose of this study is to investigate the performance of winglets, the disagreement of predictions at the hub region of the blade is of little consequence and more attention is paid to the flow and forces closer to the tip of the blade.

(a) Normal Force

(b) Tangential Force
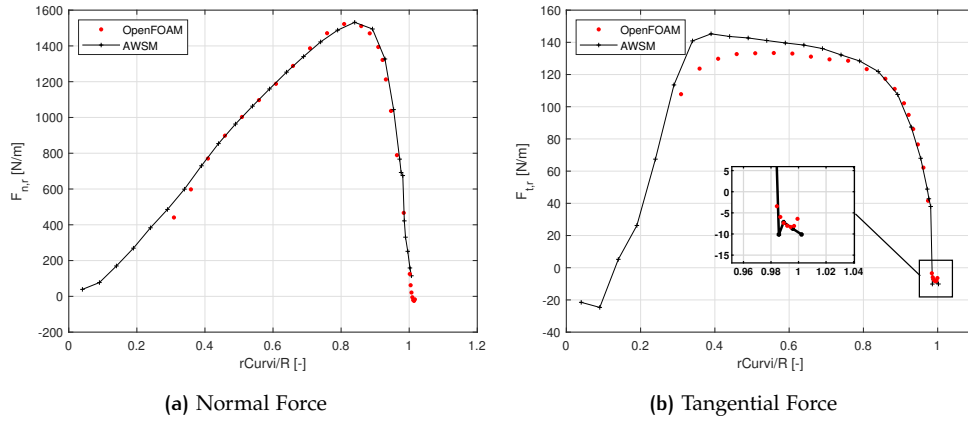
Figure 6.2: Integrated Forces wrt Rotor Plane

Focusing on the force predictions of AWSM and OpenFOAM at the winglet, normal forces, again, show good agreement with each other. The size of the winglet is very small compared to the span of the blade (i.e. 3%), and the data planes from which pressure was extracted from OpenFOAM are very close together at the tip. AWSM does not print the very last point of the blade, and thus, force data is not available for that point, but the normal forces from OpenFOAM follow the same trend as the AWSM results. For the tangential forces, there is a larger difference in the predictions of OpenFOAM and AWSM, especially at the root and tip of the winglet. Upon close inspection of the Line Integral Convolution (LIC) of the Wall Shear Stresses on Paraview, a small region of recirculation was observed at the juction between the root of the winglet and the tip of the blade (Figure 6.3). This region of complex flow would not be predicted by the vortex code, and thus a slight difference in force prediction can be expected.

Figure 6.3: Surface LIC of Wall Shear Stress at the Winglet

The circulation distribution over the span of the blade and winglet was computed using the same method explained in Chapter 5. For the winglet part of the blade, the integration curve was rotated by 90° to make it perpendicular to the winglet. The rest of the post-processing was performed in a similar way as the rest of the blade. Figure 6.4 shows the circulation distribution predicted by OpenFOAM and AWSM. A similar trend is observed as with the normal force distribution, with OpenFOAM predicting a lower value of circulation near the hub of the blade compared to AWSM. Over the outboard section of the blade, there is better agreement of circulation obtained by OpenFOAM and AWSM. The circulation distribution over the winglet is also in good agreement between the two methods.
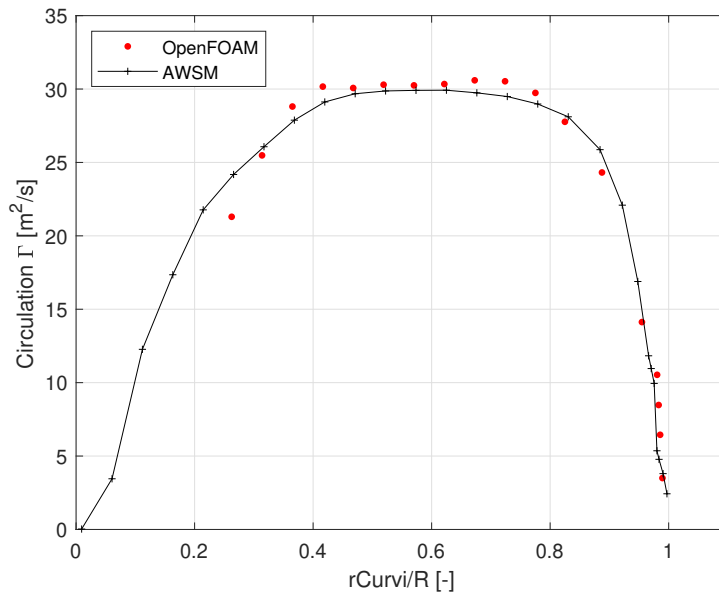
Figure 6.4: Circulation Distribution

6.2   WINGLET 2

Winglet Configuration 2 was also simulated at the same input conditions as Winglet Configuration 1, with an inlet wind velocity of $U_0 = 6.1m/s$ and a rotor speed of $12.3RPM$. The winglet geometry is presented in Figure 6.5 for ready reference.

Figure 6.5: Winglet Configuration 2 Geometry

The blade, however, operated at a different operating point compared to Winglet 1 because the total rotor radius of this configuration is smaller than the baseline and Winglet 1, and thus, operates at a lower Tip Speed Ratio (TSR). Figure 6.6 presents the normal and tangential force distribution obtained from both OpenFOAM and AWSM oriented with respect to the rotor plane.

(a) Normal Force

(b) Tangential Force
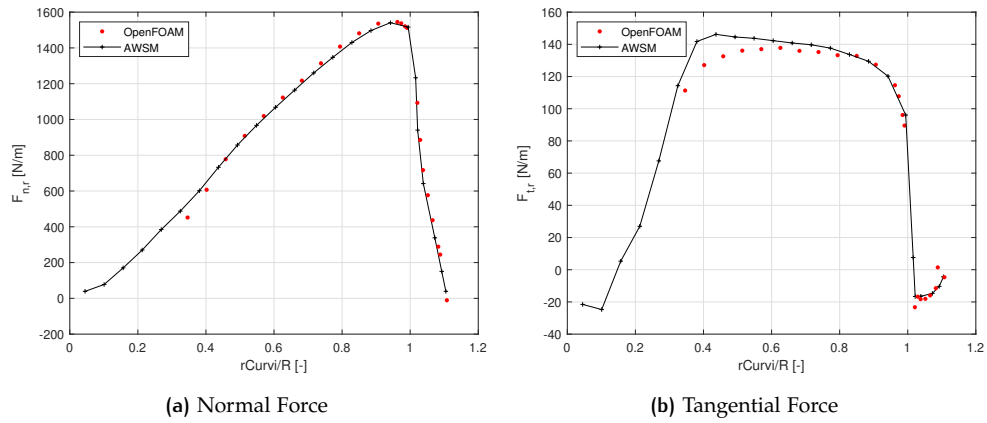
Figure 6.6: Integrated Forces wrt Rotor Plane

The observations in force predictions of both OpenFOAM and AWSM are consistent with those of Winglet Configuration 1 over the main part of the blade, except at the tip. This is expected because the setup of the models have not been modified in these regions, and would behave the same under the same input conditions. Near the winglet region, normal forces agree closely with each other between the OpenFOAM and AWSM results. A region of flow recirculation is observed at the junction between the tip of the blade and the root of the winglet, similar to the case in Winglet 1 (Figure 6.7). As a result, there is a small difference in the tangential force obtained from OpenFOAM and that from AWSM. Over the rest of the winglet, a good agreement is observed.
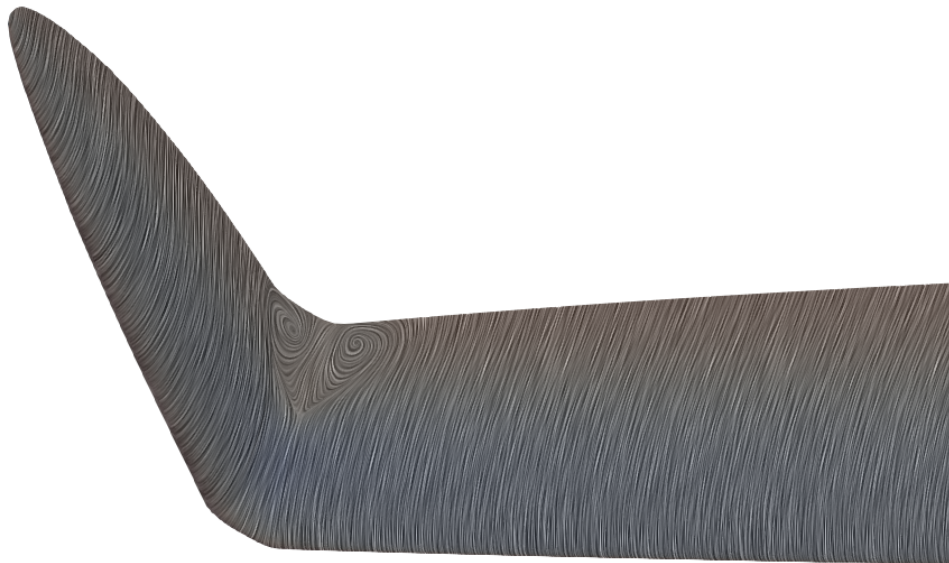
Figure 6.7: Surface LIC of Wall Shear Stress at the Winglet

Figure 6.8 shows the plot of the circulation distribution over the blade and the winglet for both OpenFOAM and AWSM. Again, similar conclusions can be drawn from the observation of circulation distribution over the main part of the blade as Winglet 1. Over the winglet, the circulation distribution is consistent with the

corresponding normal force distribution, with AWSM showing good agreement with OpenFOAM results.
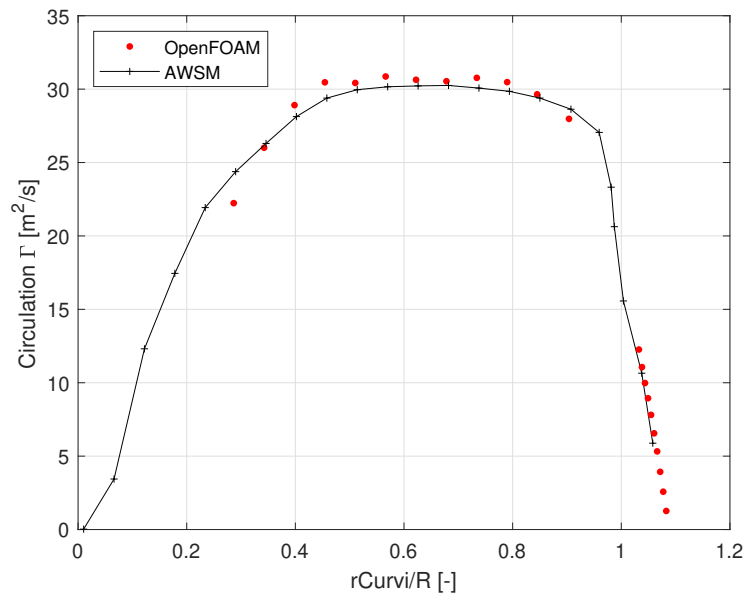
Figure 6.8: Circulation Distribution

6.3 WINGLET 3

The final configuration tested was the Winglet 3, featuring a 45 degree cant angle and total length of the blade along the pitching axis the same as the baseline blade. The winglet geometry is presented in Figure 6.9 for ready reference.

Figure 6.9: Winglet Configuration 3 Geometry

In general similar observations are made for the normal and tangential forces in the inboard regions of the blade, with forces predicted by AWSM slightly higher near the hub of the blade because of the use of transitional airfoil polars (Figure 6.10). Closer to the tip, good agreement is observed between OpenFOAM and AWSM.

(a) Normal Force
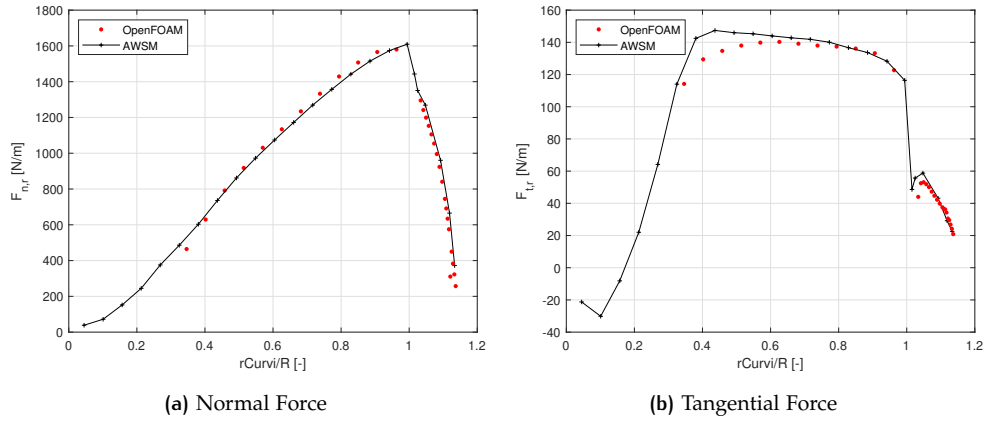
(b) Tangential Force

Figure 6.10: Integrated Forces wrt Rotor Plane

The normal forces predicted by AWSM closely match the results from Open-FOAM for the whole span of the winglet. OpenFOAM prediction of tangential forces near the junction between the winglet and the blade are slightly lower compared to results from AWSM. This is again because of the formation of a recirculating flow region at this location near the trailing edge of the blade. The tangential force results over the rest of the span of the winglet show good agreement between OpenFOAM and AWSM.

Figure 6.11 shows the circulation distribution over the blade obtained from AWSM and OpenFOAM. The distribution of circulation over the main part of the blade is similar to the baseline case, as expected. Over the span of the winglet AWSM shows close agreement with circulation computed from OpenFOAM data.
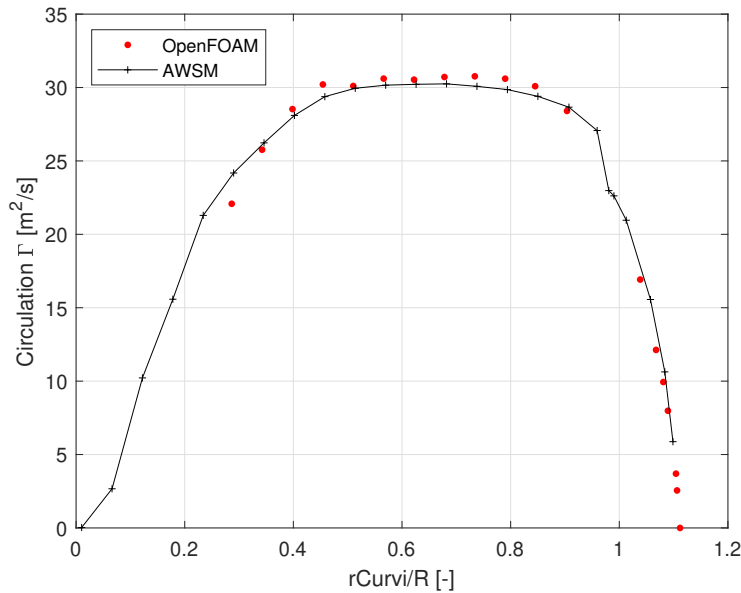
Figure 6.11: Circulation Distribution

7 | CONCLUSIONS AND RECOMMENDATIONS

This chapters draws conclusions on the discussion from the previous sections with respect to the formulated research questions. In addition, based on the outcomes of this thesis, recommendations are made for further work in this field.

7.1 CONCLUSIONS

This work aimed at assessing the accuracy and applicability of the Lifting Line code AWSM in the design and optimization of Winglets for a Wind Turbine. A verified and validated CFD model on OpenFOAM was used to compare and assess the performance of AWSM for several winglet designs based around the DanAero LM38.8m blade. Experimental and reference CFD data from EllipSys3D for the blade, available in the DanAero Database was used for the validation of the OpenFOAM model. The OpeFOAM case of the baseline blade showed close agreement of the normal and tangential forces with reference data, and this setup was used as a template for the setup of Winglet models.

The performance of AWSM was tested on three different winglet configurations - a 3% constant chord extension, a 7% winglet maintaining the curvilinear length of the blade the same as the baseline, and a 9.9%, 45° winglet maintaining the blade length along the pitching axis the same as the baseline blade. Equivalent geometry representations were created for AWSM and OpenFOAM and this was verified using TecPlot.

The major drawback of the Lifting Line Method is that it cannot accurately predict forces in regions of massive flow separation as seen in the hub region of the blades tested. A region of flow recirculation observed at the junction of the blade tip and winglet root cannot be predicted by AWSM and presents a limitation in the applicability of the Lifting Line Method in these regions. This effect is observed in the results, with a slight disagreement between AWSM and OpenFOAM results at the junction. However, in terms of forces, this limitation does not have a large influence, and overall, force predictions of AWSM are acceptable near the tip of the blade.

A general trend observed on all simulations is that the forces obtained from AWSM are always slightly higher compared to OpenFOAM simulations in the inboard section of the blade. The reason for this is attributed to the use of transitional polars in AWSM due to the unavailability of fully-turbulent airfoil polars.

Over the outboard section of the blade and along the winglet, there is good agreement with the normal and tangential forces obtained from AWSM and OpenFOAM. A similar observation is made for the circulation distribution over the blade and winglet, with AWSM showing promising results especially at the outboard section and over the winglet.

Based on the analysis of AWSM and CFD results, it can be concluded that the Lifting Line method performs sufficiently well in simulating the aerodynamics of

winglets for wind turbines. At a fraction of the cost of CFD, AWSM is a much cheaper alternative and is shown to produce acceptable results and can therefore be used in the design and optimization of winglets in wind energy applications to develop more efficient and powerful wind turbines.

7.2 RECOMMENDATIONS

This study was performed using a steady state RANS approach using a Moving Reference Frame (MRF). While it is true that switching the coordinate system to a rotating frame transforms the whole problem into a steady state one, it turned out to be the case that the problem was locally inherently unsteady. This was an issue mainly at the inboard section of the blade, where massive flow separation caused highly unsteady behaviour, which caused problems with the convergence of the RANS solution. It is therefore recommended an unsteady method, such as URANS or LES be used to obtain high fidelity data to compare to results from the Lifting Line Method.

The accuracy of AWSM is heavily dependent of the availability of high quality airfoil polars obtained at close to the conditions being studied. The absence of such polars was a source of uncertainty in this study. For further study in this area, it is necessary to obtain or generate appropriate airfoil data to be able to draw strong conclusions.

The winglet designs used in this thesis were not optimally designed and used on a blade that was originally not designed to be fitted with winglet. Addition of a winglet modifies the circulation distribution on the blade which may shift its optimal operating point. To be able to fully assess the positive (or negative) effects of winglets on wind turbines, the study must be combined with an optimization study so that optimal designs can be obtained and then compared for accuracy of results.

In this thesis, attempts were made to compute aerodynamic quantities of the blade such as the Angle of Attack distribution and the Induction Factor distribution from CFD data. The initial attempts made at computing these quantities showed inconsistent results compared to AWSM. Due to the limited time available, the decision was made to not proceed with this line of study for the remainder of the thesis. Therefore, only the idea is presented in this report, and not the results. This is, however, an active research field and there are several contested approaches to do this the right way. This, in itself, could be a topic for a thesis project and a deeper analysis of these methods and their correct application is needed.

BIBLIOGRAPHY

Aagaard Madsen, H., Bak, C., Schmidt Paulsen, U., Gaunaa, M., Fuglsang, P., Romblad, J., Olesen, N. A., Enevoldsen, P., Laursen, J., and Jensen, L. (2010). The dan-aero mw experiments. final report.

Anderson Jr, J. D. (2010). *Fundamentals of aerodynamics*. Tata McGraw-Hill Education.

Blazek, J. (2005). Structured finite volume schemes. *Computational Fluid Dynamics: Principles and Applications, 2nd ed.; Elsevier Science: Amsterdam, The Netherlands*, pages 210–213.

Branlard, E. (2011). Wind turbine tip-loss corrections: Review, implementation, and investigation of new models.

Cantwell, B. J. (2020). Applied aerodynamics lecture notes.

Drela, M. (2014). *Flight vehicle aerodynamics*. MIT press.

Ferrer, E. and Munduate, X. (2007). Wind turbine blade tip comparison using cfd. In *Journal of Physics: Conference Series*, volume 75, page 012005. IOP Publishing.

Gage, P. J. (1995). *New approaches to optimization in aerospace conceptual design*. PhD thesis, Stanford University.

Garcia-Ribeiro, D., Flores-Mezarina, J. A., Bravo-Mosquera, P. D., and Cerón-Muñoz, H. D. (2021). Parametric cfd analysis of the taper ratio effects of a winglet on the performance of a horizontal axis wind turbine. *Sustainable Energy Technologies and Assessments*, 47:101489.

Gaunaa, M. and Johansen, J. (2007). Determination of the maximum aerodynamic efficiency of wind turbine rotors with winglets. In *Journal of Physics: Conference Series*, volume 75, page 012006. IOP Publishing.

Gaunaa, M. and Johansen, J. (2008). Can cb be increased by the use of winglets?- or-a theoretical and numerical investigation of the maximum aerodynamic efficiency of wind turbine rotors with winglets. In *46th AIAA Aerospace Sciences Meeting and Exhibit*, page 1314.

Gaunaa, M., Paralta Carqueija, P., Réthoré, P.-E. M., and Sørensen, N. N. (2011). A computationally efficient method for determining the aerodynamic performance of kites for wind energy applications. In *Proceedings of the European Wind Energy Association Conference, Brussels, Belgium*, volume 1417.

Germano, M., Piomelli, U., Moin, P., and Cabot, W. H. (1991). A dynamic subgrid-scale eddy viscosity model. *Physics of Fluids A: Fluid Dynamics*, 3(7):1760–1765.

Grasso, F., van Garrel, A., and Schepers, G. (2011). Development and validation of generalized lifting line based code for wind turbine aerodynamics. In *49th AIAA Aerospace Sciences Meeting including the New Horizons Forum and Aerospace Exposition*, page 146.

Herbert, G. J., Iniyan, S., and Amutha, D. (2014). A review of technical issues on the development of wind farms. *Renewable and Sustainable Energy Reviews*, 32:619–641.

Hughes, T. J., Mazzei, L., and Jansen, K. E. (2000). Large eddy simulation and the variational multiscale method. *Computing and visualization in science*, 3(1):47–59.

Imamura, H., Hasegawa, Y., and Kikuyama, K. (1998). Numerical analysis of the horizontal axis wind turbine with wihglets. *JSME International Journal Series B Fluids and Thermal Engineering*, 41(1):170–176.

Johansen, J. and Sørensen, N. N. (2004). Aerofoil characteristics from 3d cfd rotor computations. *Wind Energy: An International Journal for Progress and Applications in Wind Power Conversion Technology*, 7(4):283–294.

Johansen, J. and Sørensen, N. N. (2006). Aerodynamic investigation of winglets on wind turbine blades using cfd.

Johansen, J. and Sørensen, N. N. (2007). Numerical analysis of winglets on wind turbine blades using cfd. In *European Wind Energy Congress*. Citeseer.

Kalmár-Nagy, T. and Bak, B. D. (2019). An intriguing analogy of kolmogorov's scaling law in a hierarchical mass–spring–damper model. *Nonlinear Dynamics*, 95(4):3193–3203.

Kalvig, S., Manger, E., and Hjertager, B. (2014). Comparing different cfd wind turbine modelling approaches with wind tunnel measurements. In *Journal of Physics: Conference Series*, volume 555, page 012056. IOP Publishing.

Katz, J. and Plotkin, A. (2001). *Low-speed aerodynamics*, volume 13. Cambridge university press.

Khaled, M., Ibrahim, M. M., Hamed, H. E. A., and AbdelGwad, A. F. (2019). Investigation of a small horizontal–axis wind turbine performance with and without winglet. *Energy*, 187:115921.

Kroo, I. (2005). Nonplanar wing concepts for increased aircraft efficiency. *VKI lecture series on innovative configurations and advanced concepts for future civil aircraft*.

Larsen, H. H. and Petersen, L. S. (2014). Dtu international energy report 2014: Wind energy—drivers and barriers for higher shares of wind in the global power generation mix.

Launder, B. and Spalding, D. (1974). The numerical computation of turbulent flows. computer methods in applied mechanics and energy, 3, 269–289.

Launder, B. E., Reece, G. J., and Rodi, W. (1975). Progress in the development of a reynolds-stress turbulence closure. *Journal of fluid mechanics*, 68(3):537–566.

Lawton, S. and Crawford, C. (2014). Investigation and optimization of blade tip winglets using an implicit free wake vortex method. In *Journal of Physics: Conference Series*, volume 524, page 012033. IOP Publishing.

Leenders, N. (2021). Vortex-model-based multi-objective optimization of winglets for wind turbines using machine learning.

Leung, D. Y. and Yang, Y. (2012). Wind energy development and its environmental impact: A review. *Renewable and Sustainable Energy Reviews*, 16(1):1031–1039.

Lilly, D. K. (1992). A proposed modification of the germano subgrid-scale closure method. *Physics of Fluids A: Fluid Dynamics*, 4(3):633–635.

Llorente, E. and Ragni, D. (2020). Trailing-edge serrations effect on the performance of a wind turbine. *Renewable Energy*, 147:437–446.

Menter, F. R. (1994). Two-equation eddy-viscosity turbulence models for engineering applications. *AIAA journal*, 32(8):1598–1605.

Muiruri, P. I., Motsamai, O. S., and Ndeda, R. (2019). A comparative study of rans-based turbulence models for an upscale wind turbine blade. *SN Applied Sciences*, 1(3):1–15.

Nangia, R., Palmer, M., and Doe, R. (2006). Aerodynamic design studies of conventional and unconventional wings with winglets. In *24th AIAA Applied Aerodynamics Conference*, page 3460.

Oerlemans, S. (2016). Reduction of wind turbine noise using blade trailing edge devices. In *22nd AIAA/CEAS aeroacoustics conference*, page 3018.

Øye, S. (1990). A simple vortex model–using vortex rings to calculate the relation between thrust and induced velocity at the rotor disc of a wind turbine. In *Proc. of the third IEA Symposium on the Aerodynamics of Wind Turbines, ETSU, Harwell*, pages 4–1.

Phillips, W. F. and Snyder, D. (2000). Modern adaptation of prandtl's classic lifting-line theory. *Journal of Aircraft*, 37(4):662–670.

Piomelli, U. and Balaras, E. (2002). Wall-layer models for large-eddy simulations. *Annual review of fluid mechanics*, 34(1):349–374.

Prandtl, L. (1921). Applications of modern hydrodynamics to aeronautics. *US Government Printing Office*.

Reid, J. T. and Hunsaker, D. F. (2021). General approach to lifting-line theory, applied to wings with sweep. *Journal of Aircraft*, 58(2):334–346.

Réthoré, P.-E. (2009). Wind turbine wake in atmospheric turbulence.

Roache, P. J. (1994). Perspective: a method for uniform reporting of grid refinement studies.

Roache, P. J. (1998). *Verification and validation in computational science and engineering*, volume 895. Hermosa Albuquerque, NM.

Roache, P. J. and Knupp, P. M. (1993). Completed richardson extrapolation. *Communications in Numerical Methods in Engineering*, 9(5):365–374.

Saffman, P. G. (1995). *Vortex dynamics*. Cambridge university press.

Schepers, J., Boorsma, K., A Madsen, H., Pirrung, G., Bangga, G., Guma, G., Lutz, T., Potentier, T., Braud, C., Guilmineau, E., et al. (2021). Iea wind tcp task 29, phase iv: Detailed aerodynamics of wind turbines.

Schmitt, F. G. (2007). About boussinesq's turbulent viscosity hypothesis: historical remarks and a direct evaluation of its validity. *Comptes Rendus Mécanique*, 335(9-10):617–627.

Sessarego, M., Ramos-García, N., and Shen, W. Z. (2018). Analysis of winglets and sweep on wind turbine blades using a lifting line vortex particle method in complex inflow conditions. In *Journal of Physics: Conference Series*, volume 1037, page 022021. IOP Publishing.

Smagorinsky, J. (1963). General circulation experiments with the primitive equations: I. the basic experiment. *Monthly weather review*, 91(3):99–164.

Spalart, P. and Allmaras, S. (1992). A one-equation turbulence model for aerodynamic flows. In *30th aerospace sciences meeting and exhibit*, page 439.

Strelets, M. (2001). Detached eddy simulation of massively separated flows. In *39th Aerospace sciences meeting and exhibit*, page 879.

Van Bussel, G. (1990). A momentum theory for winglets on horizontal axis wind-turbine rotors and some comparison with experiments. In *4th IEA Symp. on the Aerodynamics of Wind Turbines*, pages 1–18.

Van Garrel, A. (2003). Development of a wind turbine aerodynamics simulation module.

Wilcox, D. C. (2008). Formulation of the kw turbulence model revisited. *AIAA journal*, 46(11):2823–2838.

Xu, G. and Sankar, L. (2000). Effects of transition, turbulence and yaw on the performance of horizontal axis wind turbines. In *2000 ASME Wind Energy Symposium*, page 48.

Zahle, F., Sørensen, N. N., McWilliam, M. K., and Barlas, A. (2018). Computational fluid dynamics-based surrogate optimization of a wind turbine blade tip extension for maximising energy production. In *Journal of Physics: Conference Series*, volume 1037, page 042013. IOP Publishing.